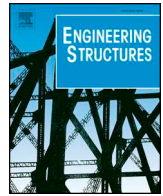




ELSEVIER

Contents lists available at ScienceDirect

Engineering Structures

journal homepage: www.elsevier.com/locate/engstruct

Seismic reliability and loss assessment of RC frame structures with traditional and innovative masonry infills

Fabio Di Trapani^a, Valentino Bolis^{b,*}, Francesco Basone^c, Marco Preti^b

^a Politecnico di Torino, Dipartimento di Ingegneria Strutturale, Edile e Geotecnica, Corso Duca degli Abruzzi, 24, 10128 Turin, Italy

^b Università degli studi di Brescia, Department of Civil, Environmental, Architectural Engineering and Mathematics, Via Branze 43, 25123 Brescia, Italy

^c Università degli Studi di Enna "Kore", Facoltà di Ingegneria e Architettura, Cittadella Universitaria, 94100 Enna, Italy

ARTICLE INFO

Keywords:

Infilled frames
Innovative sliding joint infills
Incremental dynamic analysis
Reliability
Expected annual loss

ABSTRACT

This paper presents a performance-based earthquake engineering framework aimed at the assessment of fragility, reliability and expected annual loss (EAL) of reinforced concrete (RC) frames with traditional infills (TI) and innovative infills with sliding joints (SJ). The main concern is first related to the modification of seismic reliability levels achievable for structural and non-structural limit states by code conforming RC structures when explicitly considering the influence of masonry infills and the quantification of the gain associated with the eventual use of sliding-joint infills (SJI). Further, expected annual losses within the service life are evaluated and compared for the considered structural typologies. The framework is based on the determination of fragility via incremental dynamic analysis (IDA) in order to consider statistical response to input variability. The analyses are carried out on a reference multi-storey multi-bay 2D structure modeled in OpenSEES using a fiber-section approach. Specific structural and non-structural limit states are individuated for the TI and SJI frame structures. Seismic reliability is evaluated by integrating site hazard and structural fragilities resulting for each limit state. Expected annual loss assessment is performed by directly using period dependent hazard curves to determine annual rates of failures associated with limit states. Results show that similar probabilities of exceedance and loss rates are obtained by traditional infill and sliding-joint infill structures at life safety and collapse limit states. On the contrary significant convenience in using SJI is observed for operational and damage limit states in terms of reduced probability of occurrence and EAL.

1. Introduction

Post-earthquake damage analyses have clearly shown that the share of repair costs associated with the damage of non-structural elements is dominant in frame buildings. The largest part of these costs are related to strengthening and repair of masonry infills and partition walls [1–4] which generally suffer significant damage even in the case of moderate earthquakes. In the last decade, the aim of reducing post-earthquake building restoration and downtime costs stimulated several studies on innovative infill wall solutions, conceived and designed to allow reduced or negligible damage when subjected to interstorey drifts demanded by earthquakes. In fact, traditional masonry infills offer cost effective solutions for thermal, acoustic, fire and durability performance, in many cases preferred to dry and lightweight enclosure walls. On the other hand, the drawback lays in their larger in-plane strength and stiffness associated with brittleness. The former entail large infill-frame force transmission inducing widespread damage in the masonry

and localized trusts on the frame columns, which are subject to additional combined tension and shear action [5,6] that jeopardizes their local performance. As for the latter, after reaching the peak strength, infills show in-plane and out-of-plane response degradation, with diffuse cracking and local crushing. In several cases this may evolve into out-of-plane collapse of infills, which significantly increases risk for human life [7,8]. Infill-frame interaction also occurs in case of earthquakes of moderate intensity. In these cases, even if damage is limited to the infills, this is associated with relevant repair and downtime costs. Based on these aspects, different innovative solutions to arrange masonry infills have been developed and are available in the literature. They can be summarized in two main categories, one providing infill-frame system strengthening the other providing infill-frame decoupling. The former category provides higher or more reliable strength to the infill, possibly associated with ductility (e.g. [9–12]). As for the second, the contribution of infills to the interstorey shear is significantly decreased by reducing the mutual interaction between the frame and the

* Corresponding author.

E-mail address: valentino.bolis@unibs.it (V. Bolis).

infill, in such a way that structural response is closer to that of a bare frame (e.g. [13–20]). Among infill-frame decoupling techniques, the arrangement of masonry infills with horizontal sliding joints has shown to be an effective solution for reducing infill-frame interaction forces and limiting the extent of the damage to infills even in the case of severe earthquakes. Such technique has the credit of being theoretically consolidated and experimentally confirmed [15,16,20–23]. Lateral response of sliding-joint infills has been investigated in depth by parametric analyses [24,25], while their efficiency against dynamic actions has been experimentally tested by Manzini et al. 2018 [26]. Moreover, Preti et al. 2017 [27] provided a simplified equivalent strut modelling approach effectively describing the in-plane sliding-joints infilled frame response resulting from experimental evidence.

As it can be noticed from the aforementioned studies, innovative masonry infills performance has been tested and compared with that of traditional infills both experimentally and numerically. Investigations showed promising results especially for the case of sliding-joint infills, because of their simple arrangement and damage limitation capacity, although performance of innovative solutions with respect to traditional ones has not yet been tested within a probabilistic assessment framework. In fact, the adoption of sliding infill solution, besides modifying structural fragility, provides significantly lower stiffness and increased fundamental period of the structure with respect to a traditionally infilled one. On the other hand, seismic hazard of a site, summarized by the hazard curves, is period dependent, hence it is not obvious that a lower (or higher) fragility will produce a reduction (or an increase) of the overall probability of occurrence of a limit state. In this sense, a complete comparative assessment merging seismic fragility, reliability and loss assessment during the service life can only come from a performance-based earthquake engineering (PBEE) approach, which can provide a quantification of the actual gain obtainable by adopting such kind of technological solutions. Based on this, the present paper compares the performance of code-conforming multi-storey and multi-bay frames fully infilled with traditional or sliding-joints infills using a comprehensive performance-based earthquake engineering framework. The framework is based on incremental dynamic analysis (IDA) [28] as reference tool for the determination of fragility curves, specifically defined in order to include structural and non-structural limit states. IDA curves, and the associated fragilities, are obtained by a selection of 30 ground motion records scaled, for the different systems, by assuming spectral acceleration at each specified vibration period $S_a(T_1)$ as intensity measure (IM). The proposed procedure also solves the issues of comparing fragilities of structural systems having substantially different fundamental vibration periods (e.g. traditionally infilled frames and sliding-joint infilled frames) by integrating the convolution between fragility and hazard functions. The assessment is then moved from fragility to reliability by evaluating probabilities of exceeding each limit state. The analysis results are then used to extend the investigation in terms of expected annual loss by evaluating annual frequency rates of exceeding specified limit states and allowing the estimation of post-earthquake restoration costs within the service life. Results show similar reliability of traditionally and sliding-joint infilled frames for what concerns ultimate limit states. On the contrary, reliability of sliding-joint infilled frames is significantly larger for service limit states, with a strong impact on the reduction of EAL.

2. Performance based earthquake engineering assessment framework

A performance-based earthquake engineering framework can be generally divided into four main steps: hazard analysis, structural analysis, damage analysis, and loss analysis [29]. These steps are totally generic in the PBEE concept and hence they are here specialized to properly face specific issues which are typical of the structural systems under investigation. The proposed assessment framework (Fig. 1) is specifically designed to assess seismic performance of infilled frame

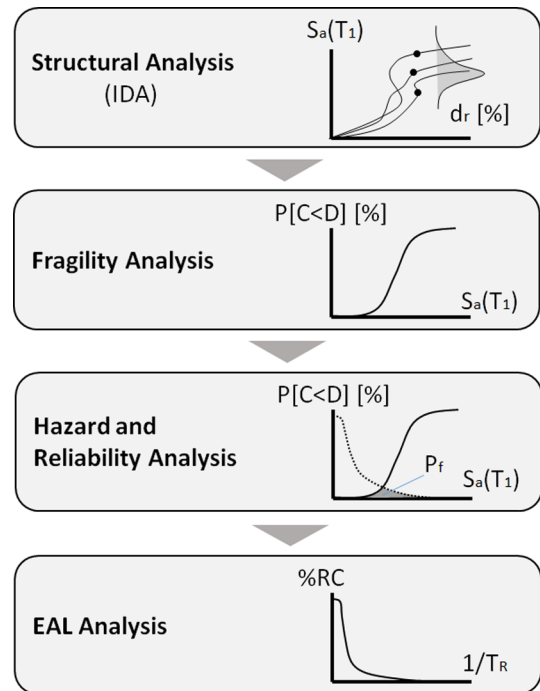


Fig. 1. Adopted performance based earthquake engineering (PBEE) framework.

systems. Single steps are described in detail in the following sections.

2.1. Structural analysis (Incremental dynamic analysis)

Incremental dynamic analyses (IDA) is adopted as reference method to get structural response. IDA has been recently widely employed by different authors (e.g. [30–33]) as it allows considering the uncertainty related to ground motions variability by obtaining a statistical distribution of the intensity measures inducing a limit state. In the current IDA framework, a set of 30 ground motions is scaled in amplitude up to the achievement of the specified limit states defined as limit engineering demand parameters (EDPs) (maximum interstorey drifts) or achievement of structural performances during the analyses (damage or collapse mechanisms) (Fig. 2a). The ground motions set is first selected based on a spectrum compatibility criterion with respect to the site target spectrum. Selected ground motions are then scaled with respect to the spectral acceleration attained in correspondence of the fundamental vibration period (T_1) of each analyzed structure, in such a way that $S_a(T_1) \cdot T_1$ is a common point for each spectrum. The obtained spectra, and the associated records, are then scaled up and down. Time history analyses are run for each ground motion at every scaling factor. The application of the ground motion selection and scaling is described in detail in Section 5. IDA curves will provide the relationship between $IM = S_a(T_1)$ and damage measure (DM) assumed as the maximum interstorey drift at the achievement of structural performance.

2.2. Fragility analysis (derivation of fragility curves)

Results of IDA allow deriving fragility curves expressing the probability of exceeding a specified limit state as a function of a specified IM. Fragility curves can be represented using a lognormal cumulative distribution function (e.g. [34]) using the following analytical expression:

$$P[C \leq D | IM = x] = \Phi\left(\frac{\ln(x) - \mu_{\ln x}}{\sigma_{\ln x}}\right) \quad (1)$$

where $P[C \leq D | IM = x]$ the probability that a ground motion with $IM = x$ will cause the achievement of a limit state, Φ is the standard

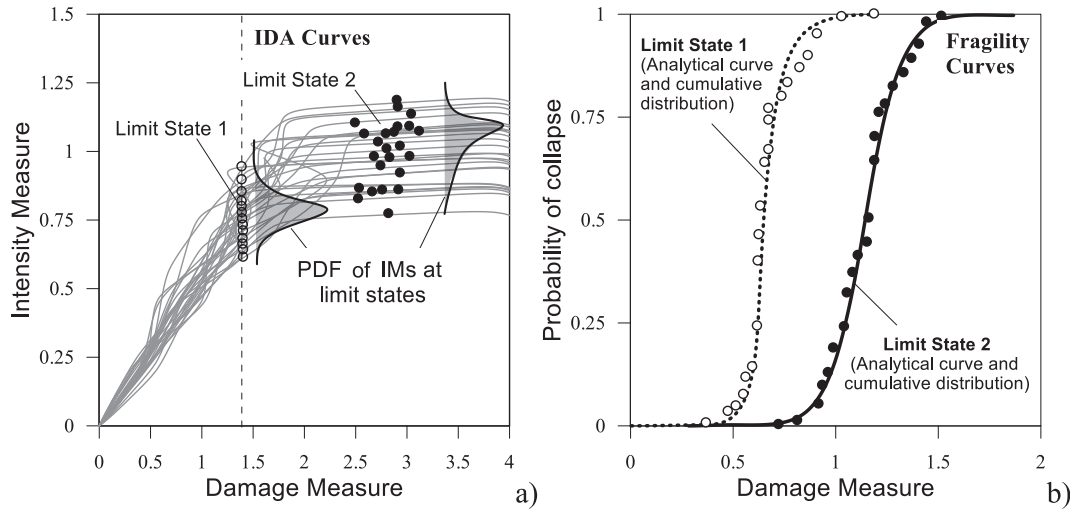


Fig. 2. Sample of determination of fragility curves for different limit states: (a) Determination of Probability density functions of IMs on IDA curves; (b) Analytical fragility curves and cumulative distributions.

cumulative distribution function, $\ln(x)$ is the natural logarithm of the variable x representing the intensity measure ($S_a(T_I)$) and $\mu_{\ln x}$ and $\sigma_{\ln x}$ are the mean and the standard deviation of the natural logarithms of the distribution of x , respectively. Fragility curves are derived for each monitored limit states during IDA (Fig. 2b). The definition of limit states for the investigated structures will be described in the following sections.

2.3. Hazard and reliability analysis

Reliability analysis allows evaluating the probability of exceeding (P_f) a given limit state in a reference time period (in years) by integrating the convolution of structural fragility curves and hazard curves. While the former represents the probability of a specific structure of period T_I to exceed a specified limit state, given the intensity, the latter describes the probability of exceeding the intensity $S_a(T_I)$ in a specific site in the reference service time period (Δt). The probability of exceeding a limit state in the reference period (P_f) can be expressed as:

$$P_f = \int_0^{+\infty} P[C \leq D | IM = x] P[x] dx \quad (2)$$

where $P[x]$ is the probability of exceeding an $IM = x = S_a(T_I)$ in a specific site in the reference period (50 years) described by a Poisson model as:

$$P[x] = 1 - e^{-\lambda[x]\Delta t} \quad (3)$$

in which $\lambda[x]$ is a function describing the annual rate of exceeding the $IM = x = S_a(T_I)$. $\lambda[x]$ hazard curves are obtained in a simplified way from spectral ordinates at different vibration periods ($S_a(T_{1,i})$) and differ return period (T_R) spectra, associated with the respective annual rates of exceedance ($\lambda = 1/T_R$). The interpolation of results allows determining the hazard curves which are site and period dependent (Fig. 3a). The convolution integral in Eq. (2) is used to determine the probability of failure (generally intended as the probability of exceeding a limit state) which takes into account both fragility and hazard. As it can be observed by Fig. 3b, a lower fragility not necessarily means lower probability of failure if fragility curves are referred to structures having different fundamental periods. At the same time the determination of P_f allows making consistent comparison between different structural systems or for the same system under different structural configurations modifying the vibration period.

2.4. Expected annual loss analysis

Expected annual loss during the reference service life is becoming a key parameter to quantify and compare the structure performances during their service life [35,36]. In this regard, loss assessment represents the last stage of the PBEE framework. This process is based on explicit determination of system performance measures meaningful to various stakeholder groups, such as monetary losses. Recently Cosenza et al. (2018) [36] provided a simplified approach to evaluate the expected annual losses (EAL) estimating the overall performance of a building in terms of earthquake-related expected economic annual loss during the reference service life. To determine EAL, it is necessary to compute the performance of the structure for each limit state in terms of capacity return period (T_{rc-LS}) and annual frequency of exceedance ($\lambda_{LS} = 1/T_{rc-LS}$), and the associated repair costs, expressed as a fraction of reconstruction costs (%RC). The advantage of this methodology is that percentage repair costs associated with each limit state, have been calibrated by Cosenza et al. 2018 [36] based on the actual repair costs monitored in the reconstruction process following recent Italian earthquakes. According to [36] the full loss or reconstruction limit state (R-LS) is assumed equal to 100%, while the %RC associated with operational limit state (O-LS), damage limit state (DL-LS), life safety limit state (LS-LS) and collapse limit state (CO-LS) are 7%, 15%, 50% and 80%, respectively. The initial damage limit state (ID-LS) is conventionally assumed having $\lambda_{ID} = 10\%$ and %RC = 0%. By connecting the points (λ_{LS} , %RC) representative of each limit state, the EAL curve is obtained (Fig. 4a). The area below the curve represents the EAL. The latter can be simply evaluated as:

$$EAL = \sum_{i=2}^5 [\lambda_{LS(i-1)} - \lambda_{LS(i)}] \cdot [\%RC_{LS(i)} + \%RC_{LS(i-1)}] / 2 + \lambda_{CO} \cdot \%RC_R \quad (3)$$

In the procedure proposed by Cosenza et al. (2018) [36] the determination of capacity return periods, which allows evaluating the annual rates of failure of each limit state (λ_{LS}), is provided by an approximated formulation based on the determination of the ratio between peak ground acceleration capacity and peak ground acceleration demand through a pushover based assessment.

In the current assessment framework, where structural analysis is performed by an IDA, it is proposed to determine λ_{LS} directly using the hazard curves obtained from the hazard analysis of the site. In detail the following steps are provided: (i) determine the distributions of IM at each limit states on IDA curves; (ii) determine fragility curves for each

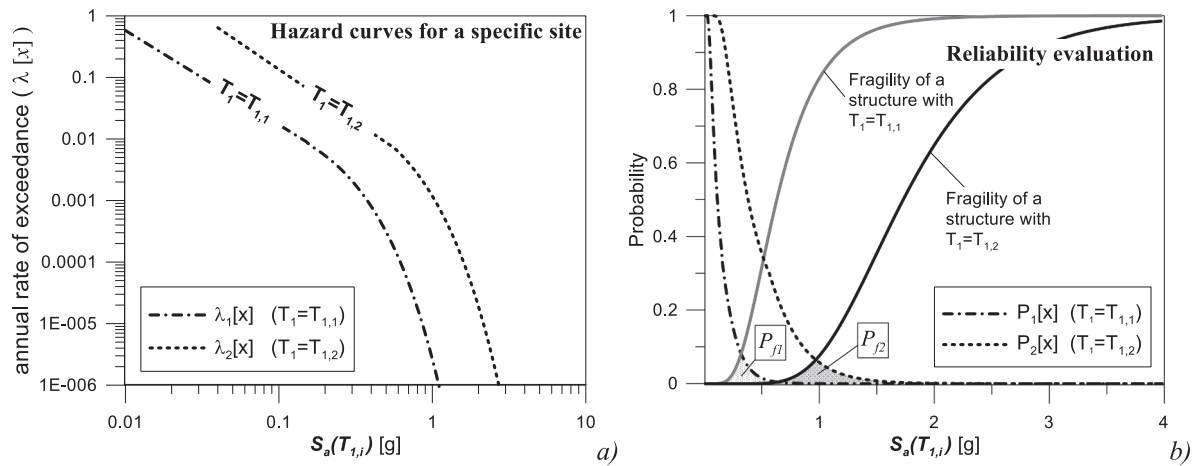


Fig. 3. Sample of hazard analysis and reliability analysis: (a) hazard curves for a specific site at two different periods (T_1 and T_2); (b) reliability assessment of two structures having periods T_1 and T_2 .

limit state and the values of the intensity measures corresponding to a 50% probability of exceedance of the required limit state performance, $\bar{S}_a(T_i)_{LS}$ (mean values); (iii) determine the corresponding annual rates of failure (λ_{LS}) through the hazard curves (Fig. 4b); (iv) build EAL curve and evaluate EAL. The choice of selecting spectral accelerations associated with 50% probability of exceedance is conventional but at the same time reasonable, since these values have the meaning of mean IM at which a LS is achieved. This procedure, besides generalizing the approach proposed by Cosenza et al. (2018) [36] to probabilistic analyses, has the advantage of directly estimating λ_{LS} from the hazard model without making use of approximate formulations.

3. The reference case study structure

3.1. Geometric and material details

The reference structure consists of a 3-bays 5-stories RC frame, extracted from a typical Italian residential building (plan view in Fig. 5a). The frame (Fig. 5b) is designed according to the Italian building code (NTC 2018 [37]) meeting the design requirements for high ductility class, considering a 6.85 kN/m^2 dead load and 0.5 kN/m^2 live load on the roof and a 7.15 kN/m^2 dead load and 2 kN/m^2 live load on the other floors. Concrete is assumed having nominal strength $f_c = 25 \text{ MPa}$, while steel rebars have nominal yielding strength $f_y = 560 \text{ MPa}$. The design for horizontal seismic forces is carried out using the design response

spectrum obtained for the city of Cosenza (soil type C) scaled by a 5.85 behavior factor, which is the maximum allowed value in Italian and European recommendations for design of moment-resisting frames in high ductility class (NTC 2018 [37], EC8 [38]). The choice of high ductility design for the structure was done to highlight and compare the different exploitation of deformation and dissipation capacity associated with the bare frame and the two different typologies of infills. Details of structural frame elements are reported in Table 1, in terms of cross-section geometry and reinforcement layout.

The frame response is analyzed considering three different configurations: bare frame (BF), infilled frame with traditional masonry infills (TI) and infilled frame with infills partitioned by horizontal sliding joints (SJ). The frame is assumed to be fully infilled by solid infills. Details of the arrangement of traditional and sliding joint infills details are illustrated in Fig. 6. Both the typologies of infills consist of a fired clay blocks masonry made of hollow blocks (Fig. 6) having 50% void ratio and 810 kg/m^3 density and a thickness (t) of 200 mm. Bed and cross joints have 15 mm thickness. Results of tests for the mechanical characteristics of materials are reported in Table 2 [22]. Traditional masonry infills are arranged as continuous masonry put in contact with the RC frame beams and columns. Sliding infills have sliding joints arranged as proposed by Preti et al. 2015 [22], with the introduction of wooden boards able to activate the sliding between two adjacent masonry sub-portions. Wooden boards are assumed to be inserted at the column-to-infill interface, in order to provide a deformable contact joint

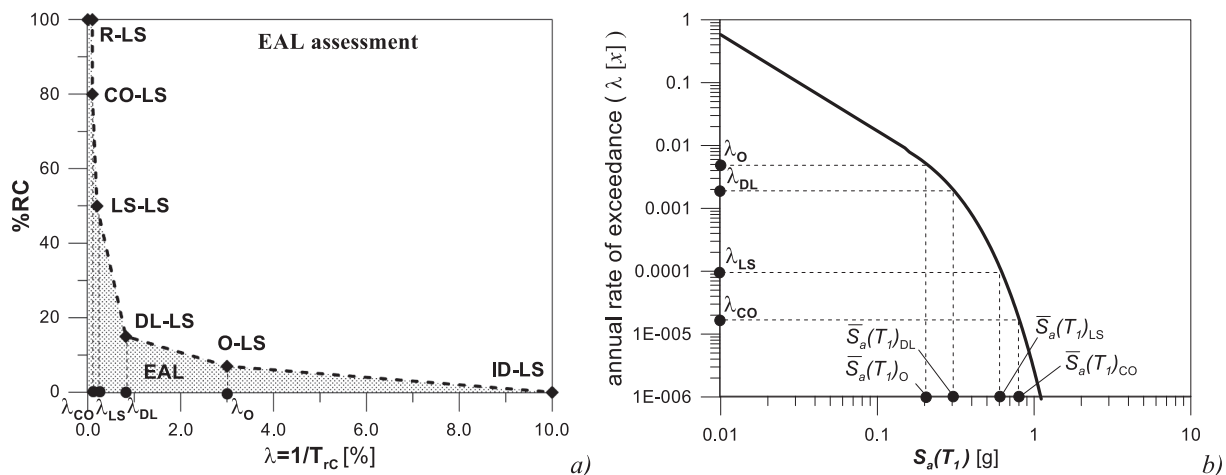


Fig. 4. EAL assessment procedure: (a) typical EAL curve; (b) determination of annual rate of failure corresponding to 50% intensity measure of the limit state (median annual rate of limit state failure).

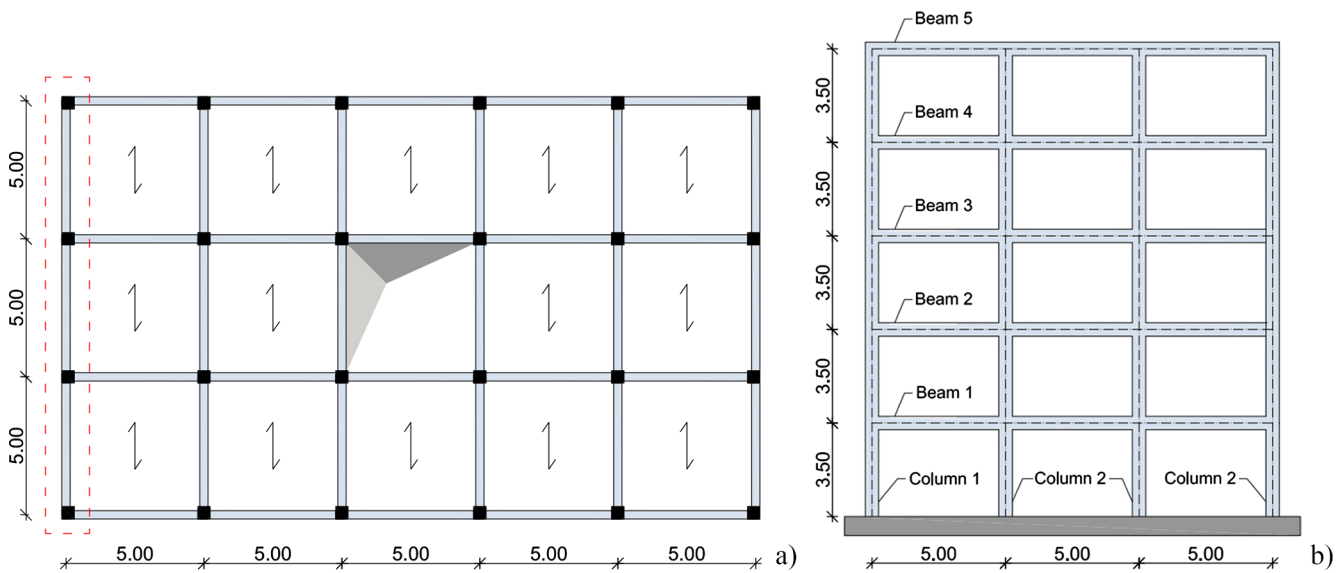


Fig. 5. Reference case study building: (a) Plan view; (b) Selected frame.

preventing masonry from crushing at the sub-panel corners. When defining the degree of interaction between sliding joint infills and the surrounding frame, a fundamental role is played by the contact joint placed at the column-to-infill interface. In particular, a reduction of the depth or yielding strength of the joint can significantly reduce contact forces transferred from the infill and the frame [39]. In the reference structure, the infill with horizontal sliding joints is considered having contact with halved depth with respect to masonry thickness (section BB in Fig. 6).

4. Structural modelling and limit states definition

4.1. Frame modeling and general assumptions

Numerical analyses on the reference structure have been performed with the OpenSEES software platform [40]. The RC frame is modeled adopting a distributed plasticity approach using fiber-section beam-column elements (Fig. 7). A “Concrete04” material stress-strain model [41,42], is attributed to the cross-section fibers. Confinement of

concrete is accounted for by dividing cross-sections into effectively confined core fiber and unconfined cover fibers [43] (Fig. 7) and elements into constant-confinement segments in such a way to account for the different transversal reinforcement. “Steel02” material model (Giuffrè-Menegotto-Pinto) is used for steel rebars. The model accounts for an isotropic strain hardening behavior [44]. The triggering of shear non-linear mechanism is not directly modeled, but possible shear damage or collapses in the frame elements are evaluated a-posteriori by comparing shear demands with corresponding capacity.

The in-plane interaction of the RC frame with masonry infills is modeled by adopting a simplified macro-element approach for both TI and SJ infills. Equivalent diagonal struts are introduced within the frame bays and calibrated in order to reproduce the infill contribution to the frame lateral strength and stiffness. The additional shear demand due to infill-frame interaction is accounted for by using an eccentric positioning of the struts. The struts are compression only truss elements accounting for the degradation during the cyclic in-plane response. The calibration of the equivalent struts of TI and SJ infills is described in detail in the following sections.

Table 1

Geometry and reinforcement details of beams and columns of the selected frame.

| BEAMS | | | | | | |
|---|---------------|---------------|----------------------------|-------------|-----------|-----------|
|  | Geometry | | Longitudinal reinforcement | | Stirrups | |
| | <i>b</i> (mm) | <i>h</i> (mm) | Bottom | Top | End-zones | Mid-zones |
| Beam 1 | 300 | 450 | 4φ20 | 2φ16 + 5φ20 | 2φ8/100 | 2φ8/150 |
| Beam 2 | 300 | 450 | 4φ20 | 2φ16 + 5φ20 | 2φ8/100 | 2φ 8/150 |
| Beam 3 | 300 | 450 | 3φ20 | 3φ16 + 3φ20 | 2φ8/100 | 2φ 8/150 |
| Beam 4 | 300 | 450 | 2φ20 | 2φ16 + 2φ20 | 2φ8/100 | 2φ 8/150 |
| Beam 5 | 300 | 350 | 2φ20 | 2φ16 + 2φ20 | 2φ8/100 | 2φ 8/150 |
| COLUMNS | | | | | | |
|  | Geometry | | Longitudinal reinforcement | | Stirrups | |
| | <i>b</i> (mm) | <i>H</i> (mm) | | | End-zones | Mid-zones |
| Column 1 | 450 | 450 | 8φ20 | | 3φ8/100 | 2φ8/150 |
| Column 2 | 450 | 450 | 8φ22 | | 3φ8/100 | 2φ8/150 |

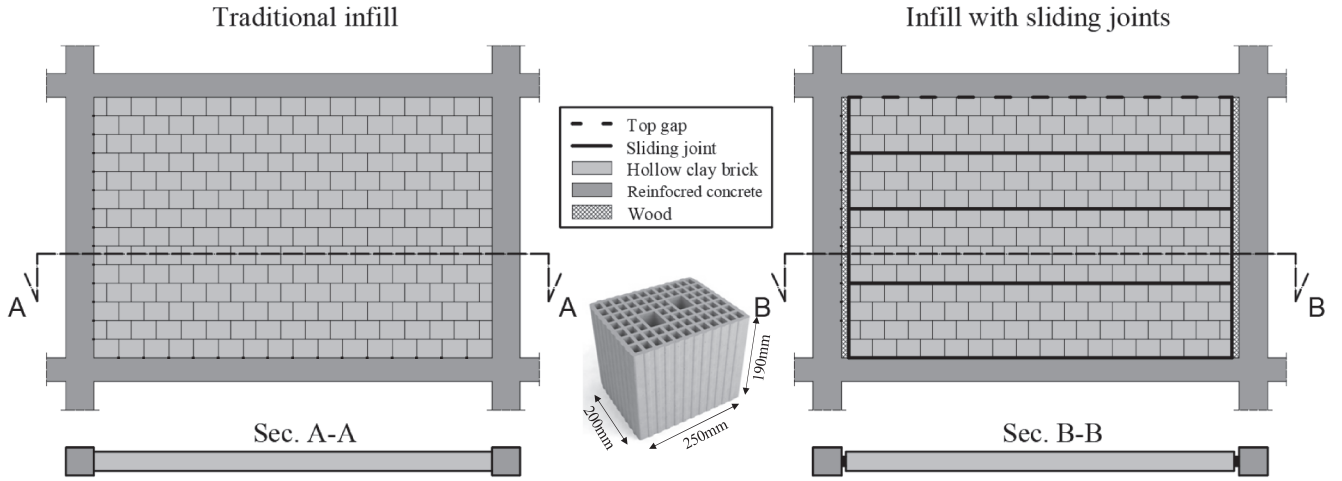


Fig. 6. Layout of traditional infills and sliding joint infills.

4.2. Modeling of traditional infills

For the traditional infill, a double strut configuration (Fig. 8) is adopted. The latter provides two parallel struts per each infill diagonal which are eccentric with respect to the beam-columns joints. Such struts are connected to the frame columns and beams at a specified distance from the joint nodes (z_c and z_b , respectively), which are quantified to reproduce the infill lateral response in terms of strength, stiffness and additional shear action induced in the frame elements. From the results of previous numerical studies [24,39] such a distance can be set as 1/10 of the frame member length, in order to provide a ratio of the maximum column shear action to infill strength of about 60%.

The calibration of struts inelastic response starts from the procedure proposed by Di Trapani et al. 2018 [33] for single equivalent strut modelling whose scheme is represented in Fig. 8. The response in compression of the struts is defined by a “Concrete02” material stress–strain model (parabolic with linear compression softening). For the single strut model, the definition of the stress–strain curve of the struts is based on the identification of the four parameters defining the stress–strain curve, namely peak stress (f_{md0}), peak strain (ϵ_{md0}), ultimate stress (f_{mdu}), and ultimate strain (ϵ_{mdu}), which are directly linked to geometrical and mechanical properties of the infilled frame by the following correlation laws [33]:

$$f_{md0} = 26.9 \tilde{f}_m \alpha^{-0.287} \quad (5)$$

$$f_{mdu} = f_{md0} (0.043\beta - 0.06) \quad (6)$$

$$\epsilon_{md0} = 3.024 \cdot \epsilon_{m0} \cdot \gamma^{0.347} \quad (7)$$

$$\epsilon_{mdu} = 0.0184 \cdot \epsilon_{md0} \cdot \delta^{-1.166} \quad (8)$$

where parameters α , β , γ and δ account for the geometrical and mechanical features of each infilled frame by the following expressions:

$$\alpha = \frac{\tilde{f}_m^2 \cdot w \cdot t}{(f_{vm} + \mu \sigma_n)^{0.2} (l/h) \cdot \lambda^{0.2}}; \quad \beta = \frac{f_{md0}^{0.7} \cdot w \cdot t}{\tilde{E}_m^{0.2} d}$$

$$\gamma = \left(\frac{f_{mdu}}{f_{md0}} \right)^2 \left(\frac{E_c}{\tilde{E}_m^{1.5}} \right); \quad \delta = \tilde{E}_m^{0.20} \cdot \epsilon_{md0} \quad (9)$$

In previous relationships ϵ_{m0} is the peak strain of masonry in compression, conventionally assumed equal to 0.0015 [45], σ_n is the average normal stress on the infill due to vertical loads (proportional to the vertical stiffness ratio between infills and columns), μ is the friction coefficient assumed equal to 0.7, E_c is the elastic modulus of concrete, d is the length of the diagonal, l and h are the length and the height of the infill, t is the actual thickness of the infill, \tilde{f}_m and \tilde{E}_m are the conventional compressive strength and elastic modulus of masonry, which are calculated as combination of the values along the two orthogonal directions (1 and 2):

$$\tilde{f}_m = \sqrt{f_{m1} \cdot f_{m2}}; \quad \tilde{E}_m = \sqrt{E_{m1} \cdot E_{m2}} \quad (10)$$

The width of the strut (w), is finally determined according to the procedure by Asteris et al. 2016 [46]. The stress-strain relationship obtained for the equivalent strut is also adopted for the two struts. Based on numerical studies (e.g. [24,47]), the shear action generated on the windward column, at the peak strength of the infill response, is about 80% of that on the leeward one. Accordingly, forces on the two struts are here calibrated so that the upper struts (A) attract larger force compared to lower ones (B). The struts section and eccentricity are calibrated by imposing the equilibrium under the following simplified assumptions: (i) the frame is considered hinged in the joints (“hinged joint layout”); (ii) the overall reaction transferred to the upper frame beam has to be equivalent to that provided by the single strut; (iii) the stiffness and strength of strut B is 80% of that in strut A. It is worth noting that the hypothesis of a frame hinged in the joints is not meant to interpret the actual mechanism activating in the real structure, but it is only assumed for a convenient calibration of the equivalent struts section and eccentricity. In fact, such assumption allows to nullify the in-plane strength of the frame and then focus on the sole infill strength contribution. Of course, the deformed shape of the frame in the model will differ from that of a hinged frame and it will vary with the imposed drift. As a consequence, the actual ratio of the strut forces in the model

Table 2
Material properties from experimental tests [22].

| Material | Compressive Strength (MPa) | Elastic Modulus (MPa) |
|--|----------------------------|-----------------------|
| Masonry prisms: Holes parallel to the load ($f_{m2} - E_{m2}$) | 7.28 | 16148 |
| Masonry prisms: Holes perpend. to the load ($f_{m1} - E_{m1}$) | 2.4 | 4408 |
| Mortar | 12.24 | 18619 |
| Wood perpend. to the grain | 2.56 | 255 |

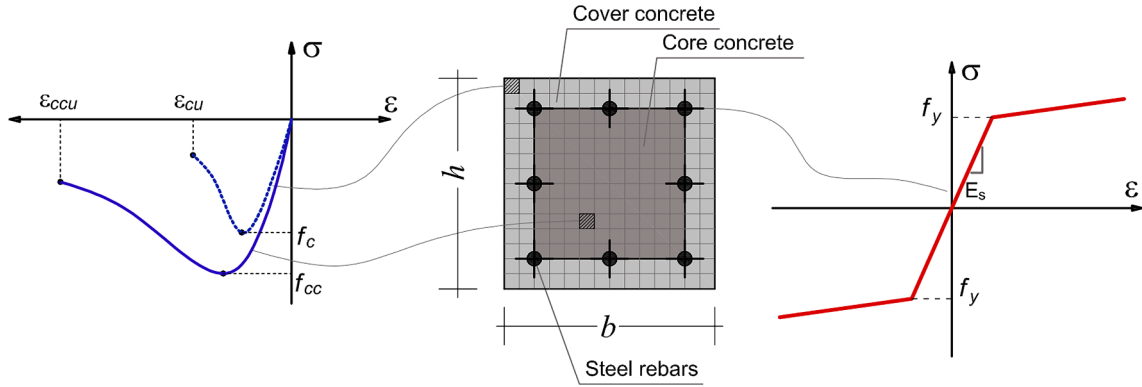


Fig. 7. Typical definition of RC frame element fiber cross-section in OpenSEES.

varies slightly with respect to the assumed value, as a function of drift. However, for the analyzed cases, such variation remains negligible (lower than 10%).

Based on previous hypotheses, if F_d is the force at a generic displacement in the equivalent strut, one can obtain the axial forces in the two parallel struts (F_{dA} and F_{dB}) as:

$$F_{dA} = \frac{F_d}{(1 + 0.8) \cdot (1 - z_c/H)} \quad F_{dB} = 0.8 \cdot F_{dA} \quad (11)$$

Given that the combination of struts has to produce the same stress-strain response as the single strut, the struts necessarily have different cross-section widths. If f_d is the generic compressive stress, and w_A and w_B the widths of struts A and B respectively, Eq. (11) can be rewritten as:

$$f_d w_A t = \frac{f_d w t}{(1 + 0.8) \cdot (1 - z_c/H)} \quad f_d w_B t = 0.8 \cdot f_d w_A t \quad (12)$$

which leads to:

$$w_A = \frac{w}{(1 + 0.8) \cdot (1 - z_c/H)} \quad w_B = 0.8 \cdot w_A \quad (13)$$

Since the two struts are parallel to the single strut, axial strains of the struts (ϵ_A and ϵ_B) are the same as of that in the single strut (ϵ). Therefore, their axial displacements (η_A and η_B) are:

$$\eta_A = \eta_B = \epsilon \cdot \sqrt{(H - z_c)^2 + (L - z_b)^2} \quad (\epsilon_A = \epsilon_B = \epsilon) \quad (14)$$

Parameters for single and double equivalent strut models are reported in Table 3.

4.3. Modeling of sliding-joint infills

Infills with sliding joints have been modeled using the strategy

proposed by Preti et al., 2017 [27]. The model provides one compression-only strut per each direction. The struts are hinged to the columns at a specified distance (z) from the frame joints. The calibration of the strut is based on closed form expressions, allowing the simultaneous prediction of the infill lateral strength (ΔF_{inf}) and maximum shear in the columns (V_{max}^{col}) at each deformation level, under the hypothesis of a hinged configuration for the frame. The force ΔF_{inf} represents the contribution of the infill to the lateral in-plane resistance of the infilled frame.

The aforementioned relationships are based on simple equilibrium considerations and depend only on the geometric and material parameters of the infill. In detail, the axial constitutive law of the strut is obtained by means of three parallel axial springs, calibrated in order to reproduce the analytically obtained force-displacement response (Fig. 9b) and the typical cyclic response of the considered infill typology. In detail, Spring 1 reproduces the contribution of the horizontal friction forces along the sliding joints, Spring 3 models the share of lateral strength offered by the diagonal struts activating in each infill sub-panel, while Spring 2 is calibrated to reproduce the increment of the friction contribution caused by the additional normal stresses on the sliding joints due to the vertical component of the strut forces in each sub-panel.

The definition of the distance z is obtained from the analytical values of the maximum infill lateral strength and the maximum shear on the columns as follows:

$$z = h \frac{V_{max}^{col} - \Delta F_{inf}}{2V_{max}^{col} - \Delta F_{inf}} \quad (15)$$

The axial force-displacement response of the springs is reproduced in OpenSEES by using the “Elasto-Plastic Gap” material, which also allows reproducing the cyclic degradation of the infill due to the progressive yielding of the contact joint when increasing the drift level

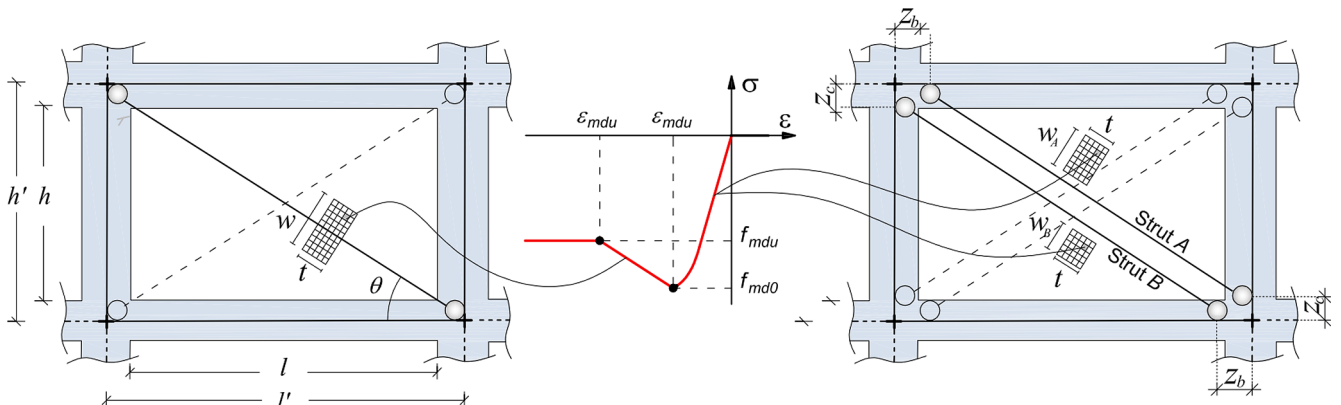


Fig. 8. Traditional infills: simplified equivalent single-strut model by Di Trapani et al. (2018) [33] and its modification into a two-struts model.

Table 3
Calibration parameters for single and double equivalent strut model for the traditional infill.

| | f_{mdo} (MPa) | f_{mdu} (MPa) | ϵ_{mdo} (-) | ϵ_{mdu} (-) | w (mm) | F_{mdo} (kN) | F_{mdu} (kN) |
|--------------|-----------------|-----------------|----------------------|----------------------|----------|----------------|----------------|
| Single strut | | | | | 1170.54 | 362.40 | 111.43 |
| Strut A | 1.548 | 0.476 | 0.00078 | 0.00733 | 722.55 | 223.70 | 68.78 |
| Strut B | | | | | 578.04 | 178.96 | 55.02 |

[24]. The calibration parameters of each strut are reported in Table 4. The layout of the reference models for the different cases is shown in Fig. 10.

4.4. Definition of structural and non-structural limit states

The four standard PBEE limit states, namely operational limit state (O-LS), damage limitation limit state (DL-LS), life-safety limit state (LS-LS) and collapse limit state (CO-LS), as defined by different building codes (NTC2018 [37], FEMA 356 [48]) are considered in the assessment framework. In particular, according to the Italian Technical code, the first two limit states are referred to damage of non-structural components (in this case the infills), while the second two identify damage of structural elements. Moreover, in order to provide more detailed individuation of limit state conditions, two further limit states are defined. One concerns the attainment of infills severe damage (ISD-LS), the other considers the frame initial damage (FID-LS) due to first yielding or first shear cracking. The standard limit states (O-LS, DL-LS, LS-LS and CO-LS) are also used for EAL assessment, adopting the conventional calibration of the percentage losses as defined by Cosenza et al., 2018 [36]. The ISD and FID limit states are instead only considered to estimate and compare their probability of occurrence during the service life.

The performance levels assumed for both the structural and non-structural limit states are summarized in Table 5. Limit state thresholds are partly based on code prescriptions and partly on the results of previous experimental studies. As regards structural limit states, collapse limit state (CO-LS) is achieved in correspondence of the first maximum interstorey drift where one of the following conditions occur: i) achievement ultimate chord-rotation (θ_u) of columns, ii) achievement of ultimate shear capacity ($V_{R,u}$) of columns, iii) achievement of 6.5% interstorey drift, after which second order effects are considered to trigger the loss of stability of the structure. Such interstorey drift limit results from the evaluation of the interstorey displacement that causes the projection of the centroid of the top column section to exit from the base column footprint. During the analyses ultimate chord rotations of columns have been evaluated by defining an axial force-chord rotation

Table 4
Calibration parameters for the parallel spring elements modeling the infill with horizontal sliding joints.

| | Spring 1 | Spring 2 | Spring 3 |
|--------------------------------|----------|----------|----------|
| Initial stiffness (kN/m) | 8239827 | 345507 | 3900 |
| Yielding Force (kN) | 37.04 | 1E-05 | 53.47 |
| Post-yielding stiffness (kN/m) | 0 | 345.51 | 687.22 |

($N-\theta$) interaction domain, in order to take into account the variation of chord rotation capacity as a function of the variation of axial force on column. The $N-\theta$ domain is defined by a fitting function interpolating θ_u values at different levels of axial load (N) [6]. Ultimate chord rotations are evaluated by means of Eurocode 8 (2004) [38] formula, which depends on both ultimate and yielding curvatures. The ultimate shear capacity $V_{R,u}$ of column is evaluated according to Model Code 2010 [49] expression. Safety coefficients for the materials have been not considered to maintain the consistency with the material models used in the analysis. The life safety limit state (LS-LS) is simply defined by the 80% of the respective θ_u and $V_{R,u}$ capacities at CO-LS. Finally, the frame initial damage limit state (FID-LS) is related to the first occurring condition between column rebars yielding (combined with flexural cracking) or initial shear cracking. The former condition is associated with the achievement of the yielding rotation (θ_y) of frame column, defined according to Eurocode 8 (2004) [38], while the first shear cracking is associated with the achievement of the resistance $V_{R,i}$ evaluated as proposed by Collins and Mitchell (1997) [50] by:

$$V_{R,i} = (0.29 \sqrt{f_c} + 0.3\sigma_{cp})b_w d \tag{16}$$

where b_w is the base width of the column, d the distance between top compressed concrete fiber and rebars in tension and σ_{cp} the compressive stress acting on the column.

For what concerns non-structural limit states, O-LS, DL-LS and IS-LS are defined as function of the interstorey drift. Interstorey drift thresholds associated to every limit state are calibrated with different values in the cases of traditional infills and sliding-joint infills, after considering results from previous experimental (e.g. [22,51]),

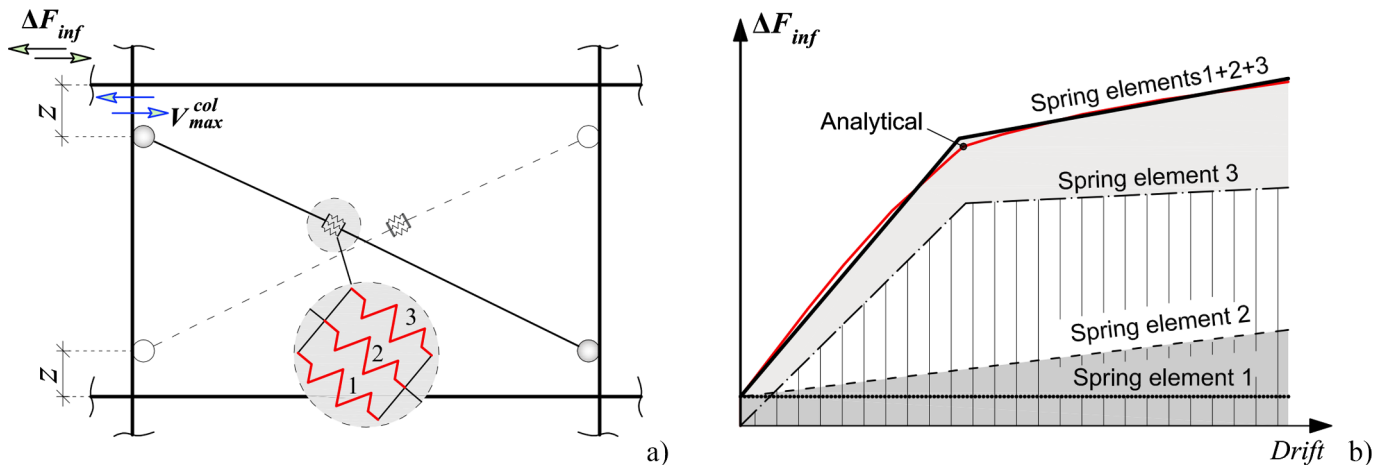


Fig. 9. Simplified equivalent strut model for the infills with horizontal sliding joints: (a) equivalent strut model for the infill with horizontal sliding joints; (b) force-drift relationships of springs.

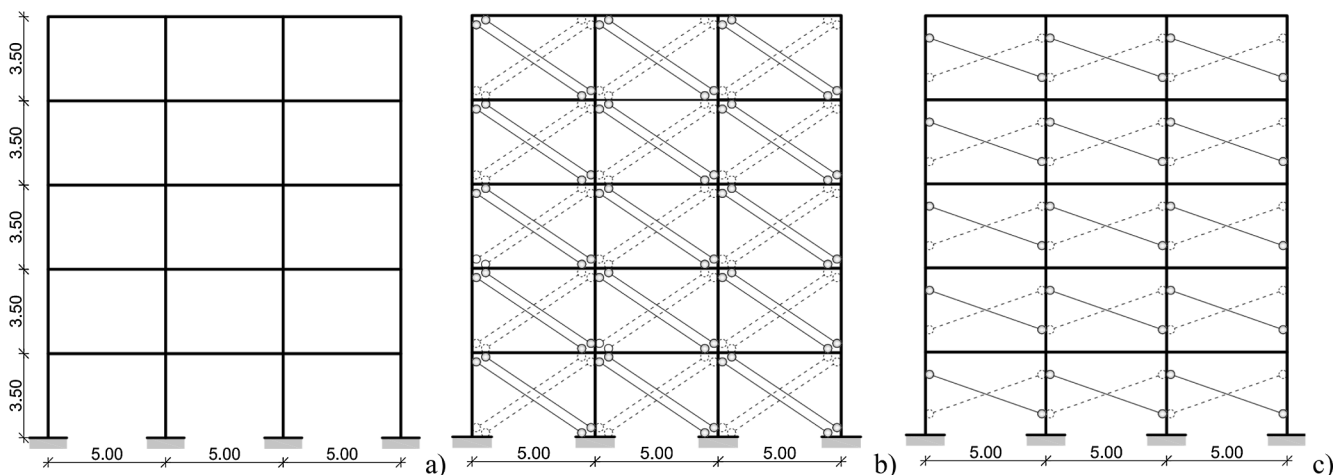


Fig. 10. Layout of the case study models: (a) bare frame; (b) traditionally infilled frame; (c) sliding-joint infilled frame.

numerical studies (e.g. [24,52]) and code provisions (EC8 2004 [37] and NTC 2018 [38]). For both the typologies of infills, the operational limit state (O-LS) defines the triggering of the first thin cracks which does not jeopardize the functionality of the building and requires a simple surface restoration. In the case of traditional infill, due to the very high stiffness, such a cracking condition is considered to be achieved for a 0.20% inter-story drift level, while the presence of horizontal sliding joints can delay the same crack pattern up to a 2.00% drift level. The damage limitation limit state (DL-LS) for the infills is defined by a more relevant damage in the masonry, which requires significant restoration interventions. According to the codes and literature review (EC8 2004 [38], NTC 2018 [38]), such a damage level is assumed to develop for a 0.50% drift in a traditional infill, while experimental and numerical studies [20,22] performed on the infill with sliding joints allow to assume for the latter solution a 3.00% drift level. Finally, the infill severe damage limit state (ISD-LS), defines a widespread damage condition of the masonry, which could also jeopardize the out-of-plane stability of the infill-wall. For traditional infills such a limit state is assumed to correspond to 1.50% drift, while for the infill with sliding joints a conventional 4.00% drift level is set, even if experimental results [20] showed not so relevant infill damage at the chosen drift. Structural and non-structural limit state thresholds for TI and SJ infills are summarized in Table 5.

5. Incremental dynamic analysis and fragility assessment

5.1. Definition of ground motions set and scaling

A set of 30 natural accelerograms was selected with the aid of the software REXEL [53] in order to respect spectrum-compatibility condition with the design spectrum of Cosenza (Italy) with soil type C and 457 years return period. In detail the NTC 2018 [37] prescription that no value of the resulting mean elastic spectrum from records, should be less than 90% of the code design spectrum was followed. A further

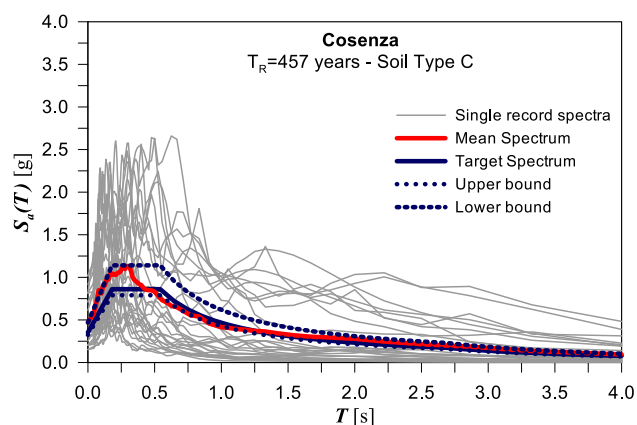


Fig. 11. Target spectrum and mean spectrum obtained from selected ground motion records.

upper bound limit for the mean spectrum values was fixed at 130% of the code design spectrum. Fig. 11 shows spectra of all the records and their mean within the upper and lower bound limits.

In order to perform incremental dynamic analysis, accelerograms are first scaled in such a way that the respective spectra assume a value of $S_a(T_1) = 0.1$ g in correspondence to the first vibration period for each considered structure. In order to select reliable conventional values for the vibration periods of the three considered structures, preliminary pushover analyses are carried out considering both modal and uniform distribution profiles for lateral forces and determining bilinear equivalent curves (Fig. 12). Vibration periods of each structure are derived from the stiffness of the elastic branch of bilinear curves by averaging results obtained for modal and uniform distributions (Table 6). This allows also considering the post-cracking period elongation. It can be observed that periods of sliding-joint infilled frames and bare frames have very similar values because of the low stiffness

Table 5 Structural and non-structural limit state thresholds for traditional and sliding joint infills.

| Limit state | Traditional infill | Limit state thresholds Sliding-joints infill | Bare Frame | Considered for EAL |
|-----------------------------|--------------------|---|------------|-----------------------|
| Non-Structural Limit states | O-LS | IDR = 0.20% | – | Yes |
| | DL-LS | IDR = 0.50% | – | Yes |
| | ISD-LS | IDR = 1.50% | – | No |
| Structural Limit states | FID-LS | | | No |
| | LS-LS | | | Yes |
| | CO-LS | | | Yes |

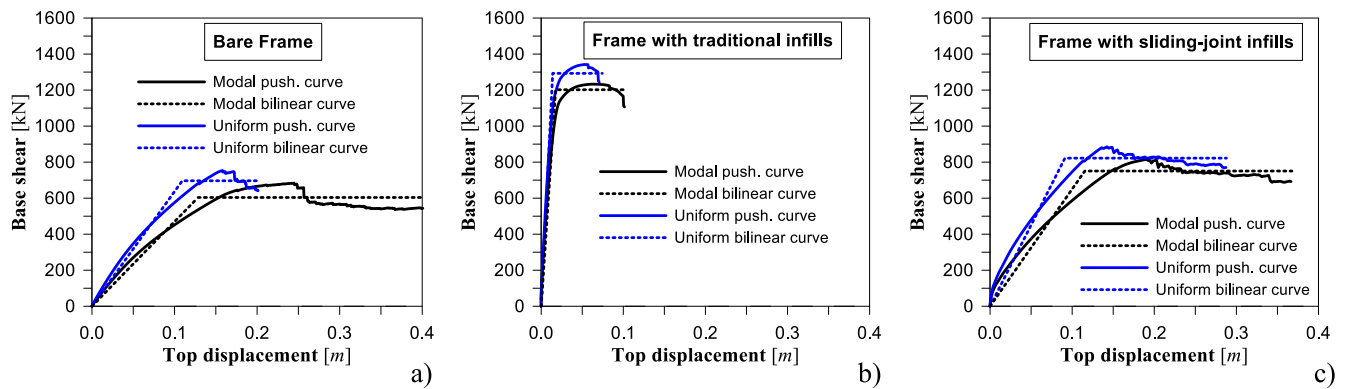


Fig. 12. Preliminary pushover tests for the determination of the average secant period of: (a) bare frames; (b) traditionally infilled frames; (c) sliding-joint infilled frames.

Table 6
Determination of reference vibration period of the structures.

| | T_1 (s) | | |
|----------------------------------|----------------------|--------------------|------|
| | Uniform distribution | Modal Distribution | Mean |
| Bare Frame | 1.70 | 1.52 | 1.61 |
| Frame with traditional infills | 0.45 | 0.40 | 0.43 |
| Frame with sliding-joint infills | 1.43 | 1.29 | 1.36 |

provided by sliding infills. Significantly lower period is instead recognized for traditionally infilled frames.

Ground motions scaled to the reference intensity of 0.1 g are shown in Fig. 13. IDA are performed for a number of scaling factors sufficient to induce all the considered limit states up to the achievement of collapse for each ground motion. The maximum scaling factors achieved were $S_a(T_1) = 1.8$ g for bare frames, $S_a(T_1) = 3.2$ g for traditionally infilled frames and $S_a(T_1) = 1.3$ g for sliding-joint infills.

5.2. IDA results and fragility assessment

IDA curves highlighting structural limit states are reported in Fig. 14. The overall trend observed shows that bare frame and sliding joint-infilled frame achieve collapse in correspondence of very similar spectral acceleration levels ($S_a(T_1) = 0.7$ g on average). Also maximum interstorey drifts recorded present similar magnitudes, ranging between 4.5% and 6.5%, which also demonstrate the trend of sliding-joint infilled frames to behave in a ductile manner, as expected by the seismically-compliant bare frame structure. A second confirmation of this is given by Fig. 15c, where it can be observed that SJ infilled frames collapsed in shear in a very few cases. A very different trend is observed for traditionally infilled frames, which present collapses at significantly higher spectral acceleration levels ($S_a(T_1) = 1.95$ g on average). This is associated with noticeable reduction of ultimate displacement capacity which highlights that in many cases collapses occur due to excess of shear demand caused by the strong infill-frame interaction. This is clearly highlighted in Fig. 15b, which shows that TI frames collapsed in shear for the majority of cases. Because of this, TI IDA curves present very large dispersion of results, especially in terms of ultimate drifts, which are concentrated around 2% in case of shear collapses, and around 5.5% in case of chord-rotation exceeding collapses. As regards frame initial damage limit state, this is achieved in correspondence of similar IM for the cases of BF and the SJ infilled frame. However, in the last case, FID-LS occurs at interstorey drift levels which are halved with respect to the BF case. This is due to the fact that first shear cracking is anticipated because of the interaction with the sliding infill. This trend results significantly amplified for the case of traditionally infilled

frames, where FID-LS occurs at about 0.5% IDR because of the very large stiffening action exerted by traditional infills.

IDA curves highlighting non-structural limit state points are reported in Fig. 16. It can be observed that O-LS and DL-LS occur at similar IM intensities for SJ and TI frames, but, in the last case, interstorey drift limits are dramatically lower. ISD-LS is achieved at about $S_a(T_1) = 1.5$ g for the TI frame. The same LS is attained for a halved IM in case of SJ infilled frames, however, this is associated with a 4% IDR, highlighting that severe damage of SJ infills occurs in correspondence of drift levels close to those inducing collapse.

The base-shear vs. first interstorey drift response of the three considered structures is reported in Fig. 17 for a single ground motion at different scaling factors, which correspond to the achievement of different limit states. Diagrams clearly highlight the reduced IDR thresholds where non-structural limit states are attained in the case of traditional infills with respect to the case of sliding-joint infills, which instead results in the same order of magnitude of those achieved by bare frame.

Fragility curves and discrete cumulative distributions derived from the results of IDA are reported in Figs. 18 and 19 for structural and non-structural limit states respectively. For non-structural limit states only the infilled frame cases are obviously considered. The close proximity of life safety and collapse limit states indicates that their attainment occurs in a very small range of increments of the IM. This can be also observed from IDA curves, which however, show that maximum interstorey drifts reached for LS and CO are significantly different. In the case of traditional infills, fragility curves associated with the most severe structural and non-structural limit states are noticeably shifted on the right with respect to the case of sliding-joint infills. This is due to the major strength of the TI system, which requires larger lateral forces to induce limit states. However, as stated in the introductory considerations, a comparison between the performances of the two systems cannot be addressed by directly comparing fragility curves. This first because of the intensity measures, which are referred to different vibration periods. Second, and correlated to the first reason, because hazard curves are period dependent. As a consequence of this performance comparisons are made in terms of reliability as show in the following section.

6. Hazard analysis and reliability assessment

Hazard analysis has been carried for the site under investigation (Cosenza, Italy) and the specified soil stiffness (type C according to EC8 classification). Hazard curves, representing the annual rates of exceeding the $IM = S_a(T_1)$ (Fig. 20a), are obtained for each vibration period associated with the three structural typologies. In detail, hazard curves are defined as interpolation functions of single $S_a(T_1)$ - λ points (Fig. 20a), representing the values assumed by spectral accelerations at

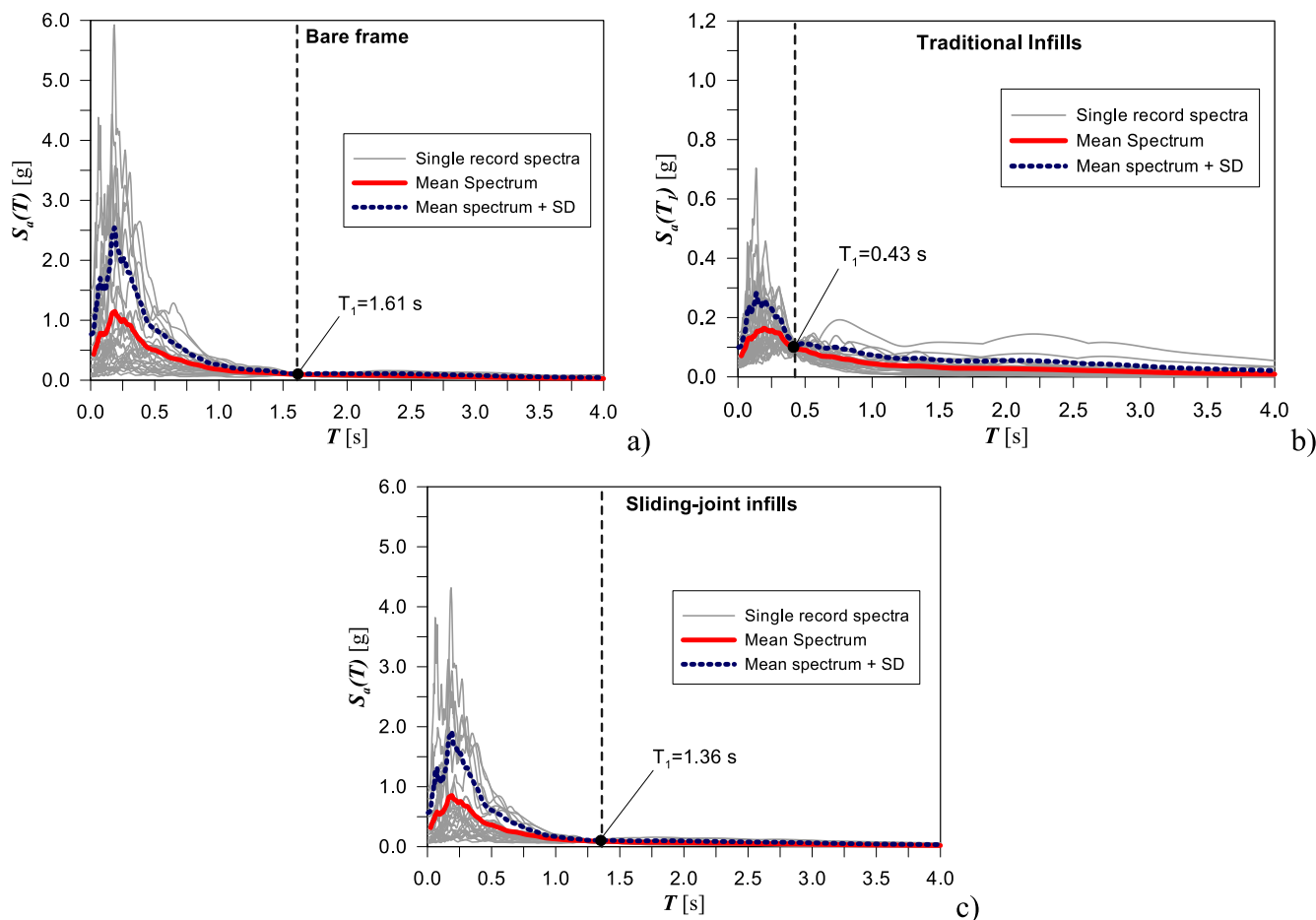


Fig. 13. Scaled accelerograms for $S_a(T_1)$: (a) bare frame, (b) traditional infills; (c) sliding joint infills.

a given structural period for different return period design spectra ($\lambda = 1/T_R$). Hazard curves are then converted into probabilities of exceedance within a service life of 50 years by using the Poisson's model equation provided in Eq. (3), where is ΔT indeed 50 years and $\lambda[x = IM]$ the interpolation function for each period. Hazard curves in 50 years for each vibration period are depicted in Fig. 20b.

Hazard curves, expressing the probability of exceedance in 50 years for the reference vibration periods, are superimposed with fragility curves of the three structural typologies (Figs. 21-22). The intersection areas between hazard and fragility curves are proportional to the probabilities of exceedance the different limit states, which are numerically determined by Eq. (2). Figs. 21 and 22 highlight the different amplitudes of the intersection areas between hazard and fragility curves. Major amplitude of intersection surfaces can be recognized for both structural and non-structural limit states in the case of traditionally infilled frames due to the major probability of exceedance associated with the respective vibration period ($T_1 = 0.42$ s).

The obtained probabilities of occurrence (P_f) for both structural and non-structural limit states are compared as bar charts in Fig. 23 and reported in Table 7. As regards life safety and collapse limit-states, the obtained probabilities of occurrence are in the same order of magnitude for the three considered cases (Fig. 23b), although the traditionally infilled frame presents slightly larger values. This result is meaningful if compared with the outcomes of fragility curves, which have shown apparent better performance of TI frames in terms of average $S_a(T_1)$ values. Noticeable differences can be instead observed for the FID-LS, where TI frames achieve a P_f of 15.02%, which results 5 times and 10 times the same probabilities evaluated for SJ infilled frame and bare frame, respectively. Such result is mainly due to the relevant shear force induced in the frame columns (because of the interaction with

traditional infills), which leads to the activation of shear cracking, even in the case of moderate intensity earthquakes. On the contrary, for the case of sliding joints infills, the reduced frame-infill interaction delays the damage to higher seismic intensities, which are associated with a lower probability of occurrence. With regards to non-structural limit states, Fig. 23a shows a dramatically reduced probability of occurrence in the cases of SJ infills with respect to TI for all the considered LS. Probabilities of occurrence of O-LS, DL-LS and ISD-LS for traditionally infilled frames are about 10 times, 13 times and 5 times the probabilities evaluated in the case sliding-joint infilled frames. The very different results obtained for non-structural limits states in the cases of traditional infills and sliding-joint infills is justified by the combination of two main factors. First the reduced stiffness and shear interaction of SJ infills allows the attainment of non-structural LS at significantly larger drifts with respect to the case of TI frames. Second, the vibration period of the SJ infilled frame is close to that of the bare frame and noticeably longer with respect to that of the TI frame. This results in a significantly lower hazard expressed by the specific hazard curve, which strongly affects the calculation of the probability of occurrence through Eq. (2). For all the considered cases, P_f values can appear higher with respect to the standard reliability levels expected by code conforming buildings. However, given the very high hazard level of the site, this result is in line with the findings highlighted by Iervolino et al. (2018) [54], demonstrating that despite the homogeneity of design actions, seismic reliability tends to decrease with the increase of seismic hazard of the sites.

7. Loss assessment

Expected annual loss assessment has been carried out using the

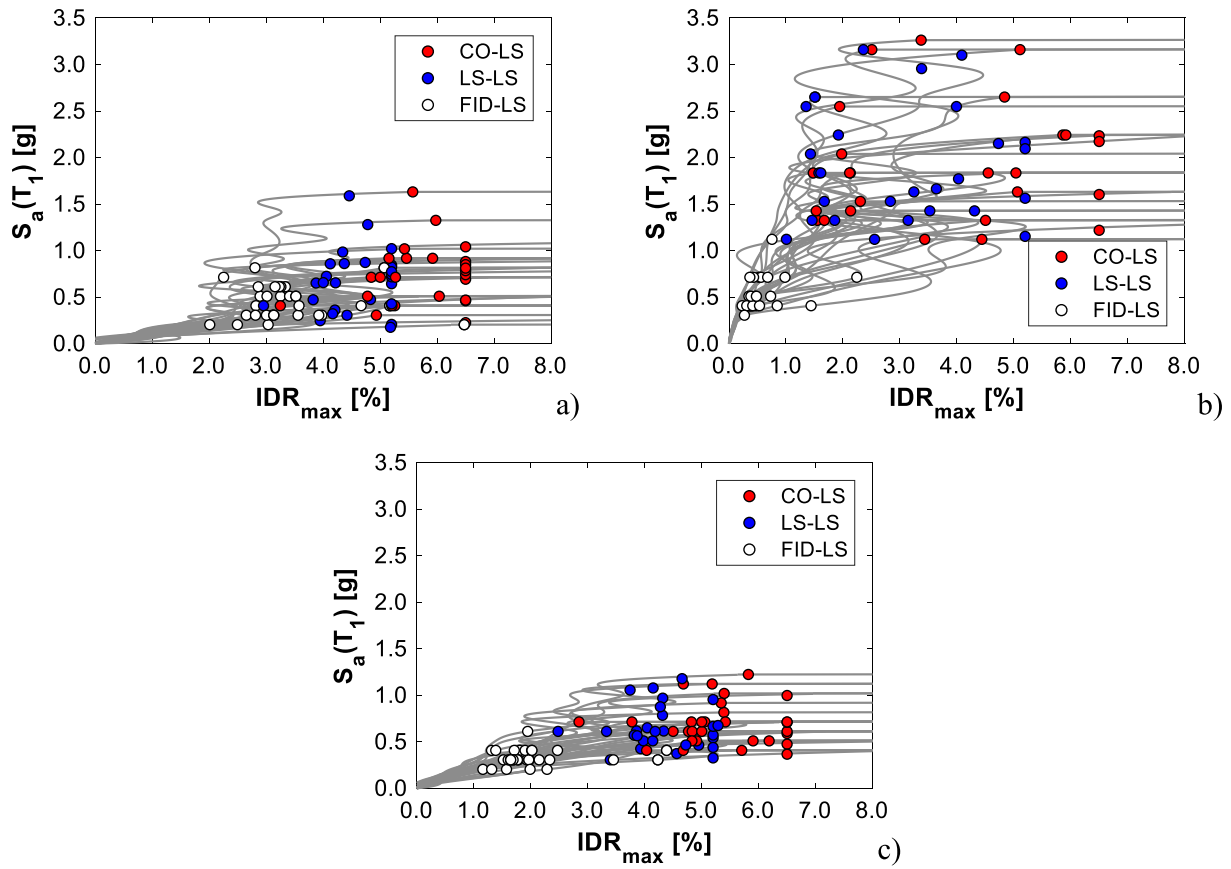


Fig. 14. IDA curves and structural limit state points for: (a) bare frame, (b) traditionally infilled frame; (c) sliding-joint infilled frame.

procedure by Cosenza et al. (2018) [36] updated as illustrated in section 2.4. Loss assessment considered only the standard limit states for structural components (LS-LS and CO-LS) and non-structural components (O-LS and DL-LS). As described in section 2.4, the annual rates of exceeding the limit states are obtained from hazard curves ($\lambda[IM]$) using the spectral accelerations associated with the 50% probability of exceeding the limit states ($\bar{S}_{a-LS} = (T_i)$) expressed by the respective fragility curves. Hence λ values at the different limit states (λ_{LS}) are evaluated as:

$$\lambda_{LS} = \lambda[\bar{S}_{a-LS}(T_i)] \quad (17)$$

A graphical exemplification of this operation is provided in Fig. 24a, while λ_{LS} and $\bar{S}_{a-LS} = (T_i)$ values are reported in Table 8. The obtained λ -%RC relationships are illustrated in Fig. 24b for traditionally infilled frames and sliding-joint infilled frames. In the same diagram, the λ -%

RC curve of the code compliant structure is also reported. The latter represents the exact match between capacity and demand for each limit state and is associated to an EAL of 1.13%. The obtained expected annual loss of the sliding-joint infilled frame (0.40%) was about half of the traditionally infilled frame (0.76%). This difference is entirely due to the gain in terms of reduced λ for non-structural limit states, which is one order of magnitude lower with respect to the case of traditional infills. Both TI and SJI structures EAL is lower than the reference value of 1.13%. This confirms that, code-conforming traditionally infilled frames structures have adequate performance in terms of EAL, which allow assigning a A_{EAL} seismic risk class according to the Italian guidelines for seismic risk classification [36]. On the other hand, the adoption of sliding-joint infills, besides reducing losses during the service life, allows the achievement of the highest risk class (A_{EAL}^+).

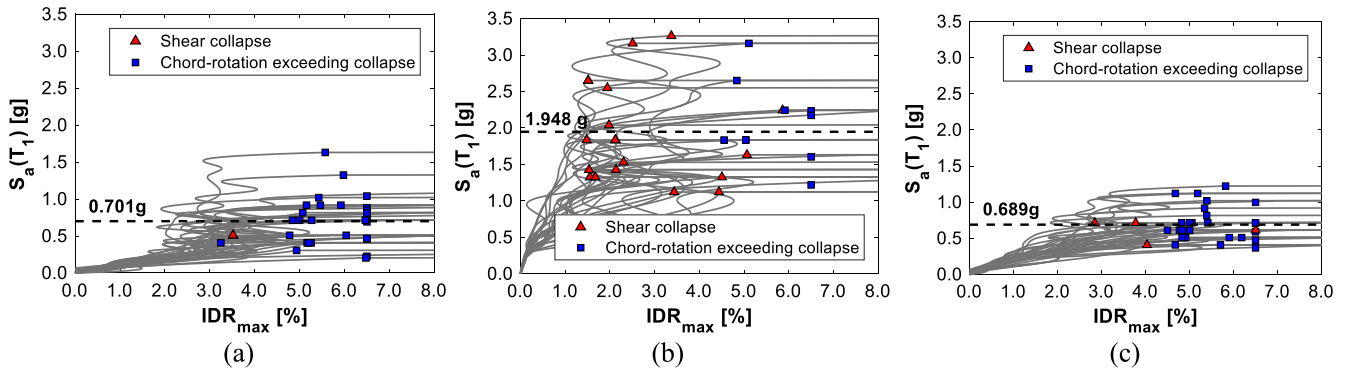


Fig. 15. Collapse modes at CO-LS on IDA curves for: (a) bare frame, (b) traditionally infilled frame; (c) sliding-joint infilled frame.

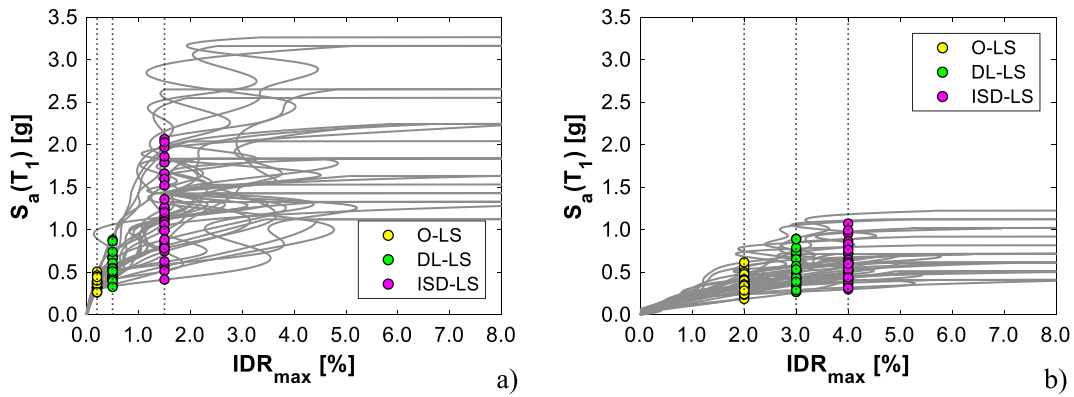


Fig. 16. IDA curves and non-structural limit state points for: a) traditionally infilled frame; b) sliding-joint infilled frame.

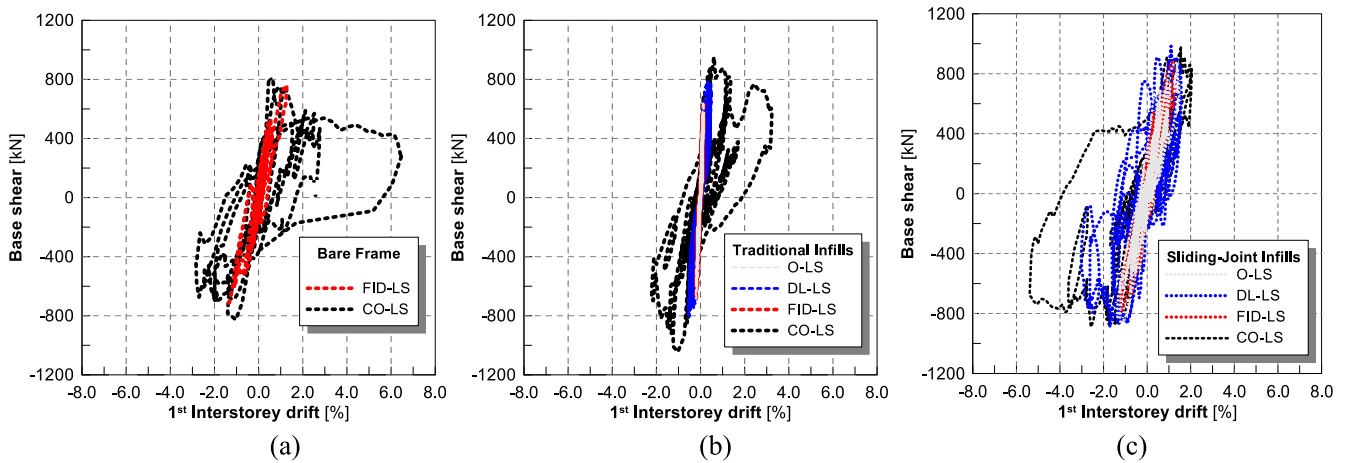


Fig. 17. Base-shear vs. first interstorey drift response for a single ground motion scaled in correspondence of the achievement of different limit states: (a) bare frame; (b) traditionally infilled frame; (c) sliding-joint infilled frame.

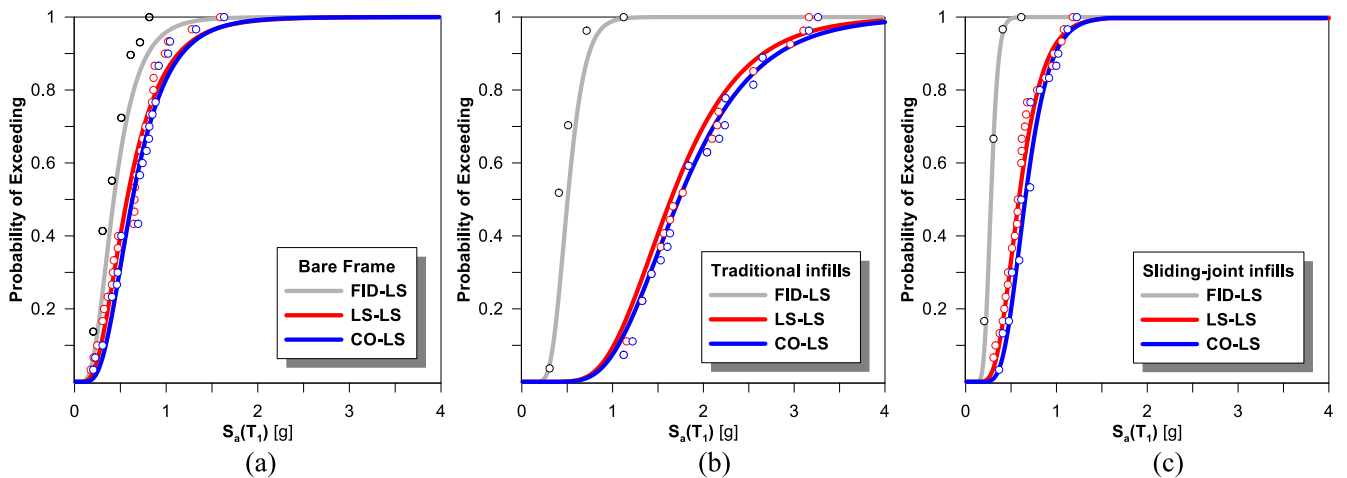


Fig. 18. Analytical fragility curves and cumulative distributions of structural limit states for: (a) bare frame; (b) traditionally infilled frame; (c) sliding-joint infilled frame.

8. Conclusions

The paper presented a PBEE approach properly defined to assess and compare the performance of masonry infilled RC frames with traditional infills and innovative infills with sliding-joint sub-panels. The latter is an emerging innovative construction technique characterized by an in-plane reduced stiffness and large deformation capacity combined with low damage and large out-of-plane resistance. The adopted

assessment methodology is based on incremental dynamic analysis to consider statistical response to input variability. Specific limit state conditions have been defined to account for structural and non-structural damage due to infill-frame interaction in the cases of bare frame, traditionally infilled frame and sliding-joint infilled frame. Reliability assessment allowed comparing the performances of the systems by accounting for both fragility and hazard to obtain probabilities of occurrence of each considered limit state. Finally, loss analysis provided

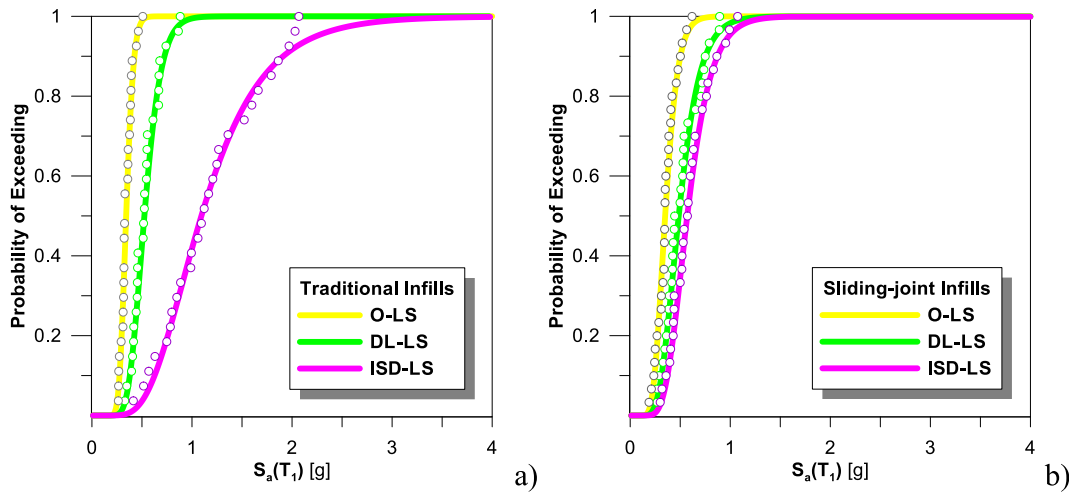


Fig. 19. Analytical fragility curves and cumulative distributions of non-structural limit states for: (a) traditionally infilled frame; (b) sliding-joint infilled frame.

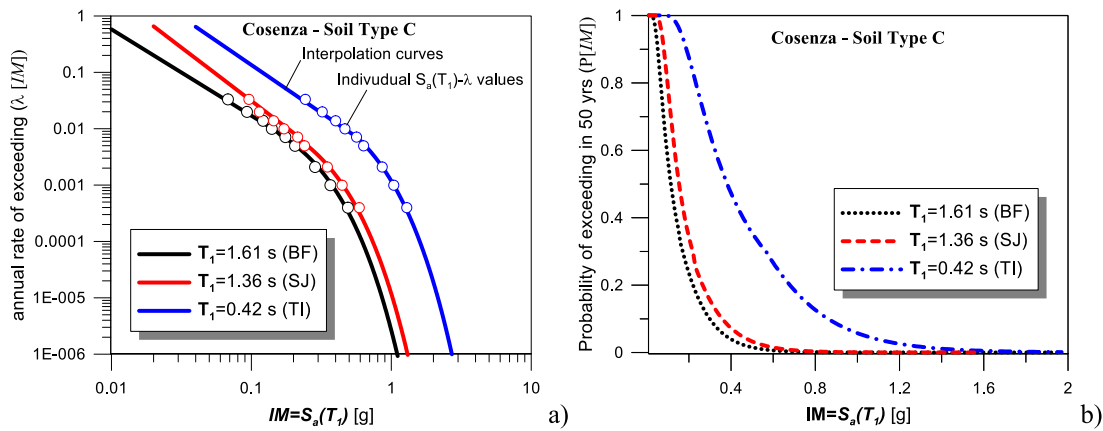


Fig. 20. Hazard analysis for Cosenza (Italy), soil Type C: (a) annual rate of exceedance curves for different T_1 values; (b) Probability of exceedance in 50 years curves for different T_1 values.

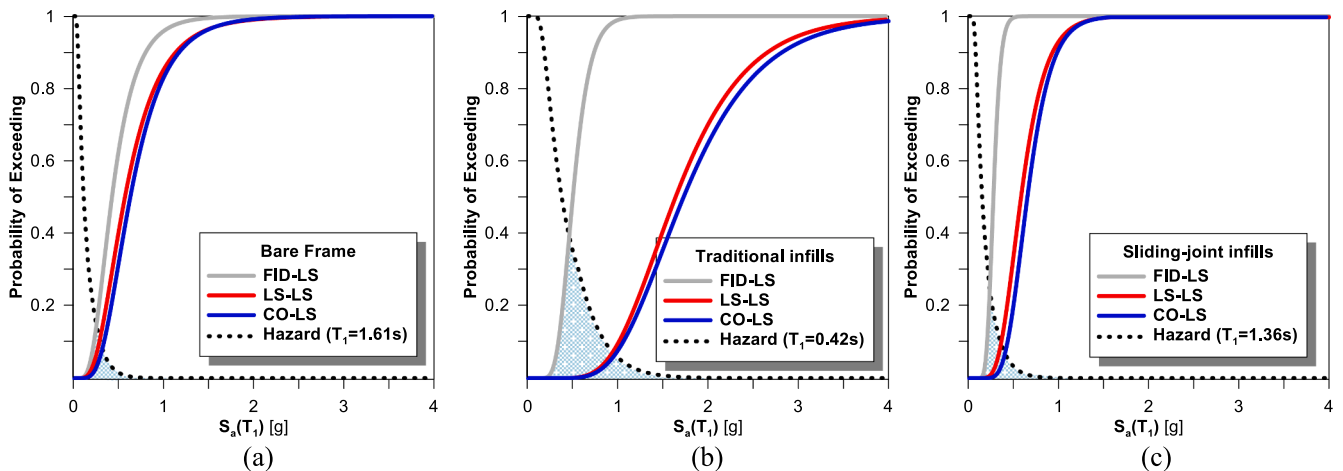


Fig. 21. Fragility curves of structural limit states and hazard curves (Cosenza, Soil Type C) for: (a) bare frame; (b) traditionally infilled frame; (c) sliding-joint infilled frame.

the expected annual losses during the service life for the different infilled frame typologies. Based on the obtained results, the following conclusions can be drawn:

- Sliding-joint infilled frame tends to behave similarly to the bare frame in terms of strength, stiffness and recognized failure modes.

This is clearly observable by IDA curves, which also highlighted that, on the contrary, traditional infills (TI) significantly increased the overall resistance but, in a significant number of cases, induced brittle shear failures due to the large shear demand related to the stronger infill-frame interaction.

- Similar probabilities of occurrence have been evidenced for life

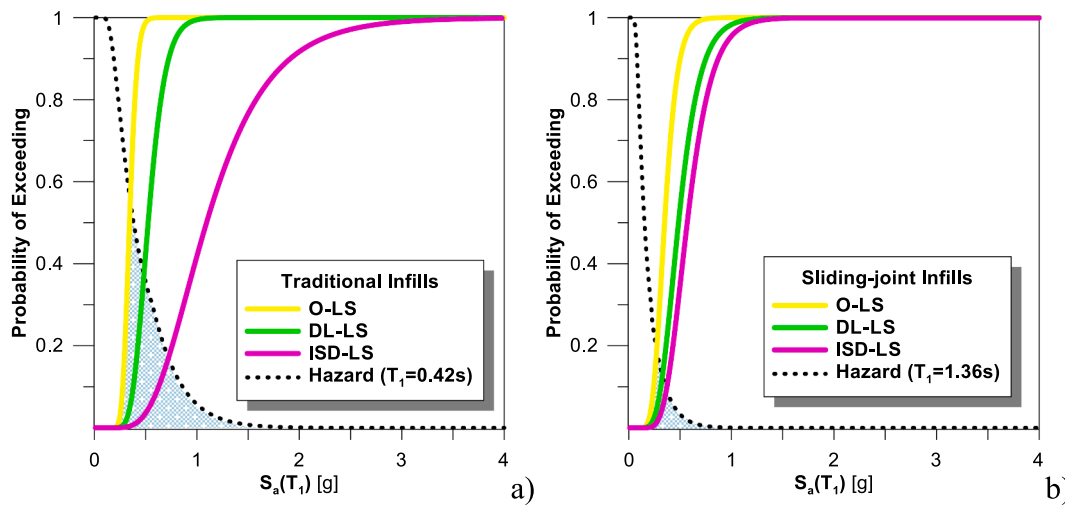


Fig. 22. Fragility curves of non-structural limit states and hazard curves (Cosenza, Soil Type C) for: (a) bare frame; (b) traditionally infilled frame; (c) sliding-joint infilled frame.

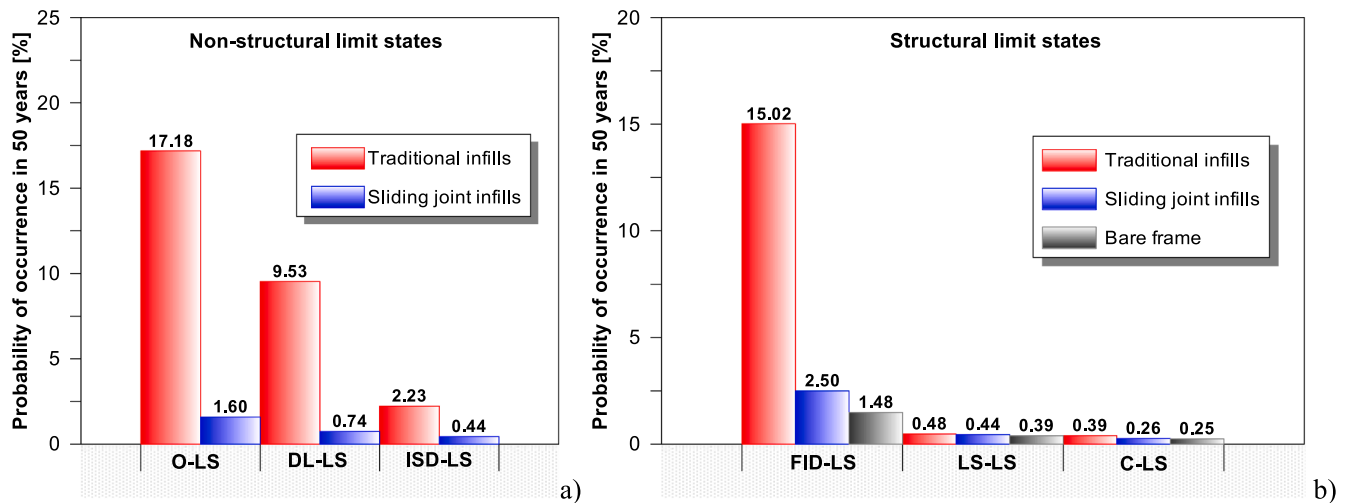


Fig. 23. Probabilities of occurrence in 50 years of limit states for the different structures: (a) non-structural limit states; (b) structural limit states.

Table 7
Probabilities of occurrence of limit states for the different structures.

| | | Probabilities of failure P_f (-) | | |
|-------------------|--------|------------------------------------|-----------------------|-----------------------|
| | | Bare Frame | Traditional Infills | Sliding-joint infills |
| Non-structural LS | O-LS | - | 1.72×10^{-1} | 1.60×10^{-2} |
| | DL-LS | - | 9.53×10^{-2} | 7.41×10^{-3} |
| | ISD-LS | - | 2.23×10^{-2} | 4.41×10^{-3} |
| Structural LS | FID-LS | 1.48×10^{-2} | 1.50×10^{-1} | 2.50×10^{-2} |
| | LS-LS | 3.92×10^{-3} | 4.77×10^{-3} | 4.45×10^{-3} |
| | CO-LS | 2.49×10^{-3} | 3.95×10^{-3} | 2.61×10^{-3} |

Table 8
 $\bar{S}_{a-LS} = (T_1)$ and λ_{LS} values at the different limit states and EAL values for TI frames and SJI frames.

| | Traditional Infills | | | Sliding-joint infills | | |
|-------|------------------------------|-----------------------|---------|------------------------------|-----------------------|---------|
| | $\bar{S}_{a-LS} = (T_1)$ [g] | λ_{LS} | EAL [%] | $\bar{S}_{a-LS} = (T_1)$ [g] | λ_{LS} | EAL [%] |
| CO-LS | 1.73 | 5.76×10^{-5} | 0.76 | 0.66 | 1.84×10^{-4} | 0.40 |
| LS-LS | 1.64 | 8.36×10^{-5} | | 0.59 | 3.24×10^{-4} | |
| DL-LS | 0.52 | 8.21×10^{-3} | | 0.49 | 7.27×10^{-4} | |
| O-LS | 0.34 | 1.69×10^{-2} | | 0.35 | 2.25×10^{-3} | |

safety and collapse limit states for the three considered cases, although fragility curves of TI frames apparently showed better performance. On the contrary, the major differences in terms of reliability were highlighted for non-structural limit states and for the FID-LS, for which SJI frames showed significantly reduced probability of occurrence (P_f) with respect to TI. This was due to the reduced tendency of SJI frames to undergo damage even in case of large interstorey drifts because of the limited interaction with the frame. Further, the presence of sliding-infills resulted in a significantly longer vibration period ($T_1 = 1.36$ s) with respect to that of the TI frame ($T_1 = 0.42$), very close to that of the bare frame ($T_1 = 1.61$ s). A consequence of this is that hazard curves obtained considering vibration periods characterizing bare frames and sliding

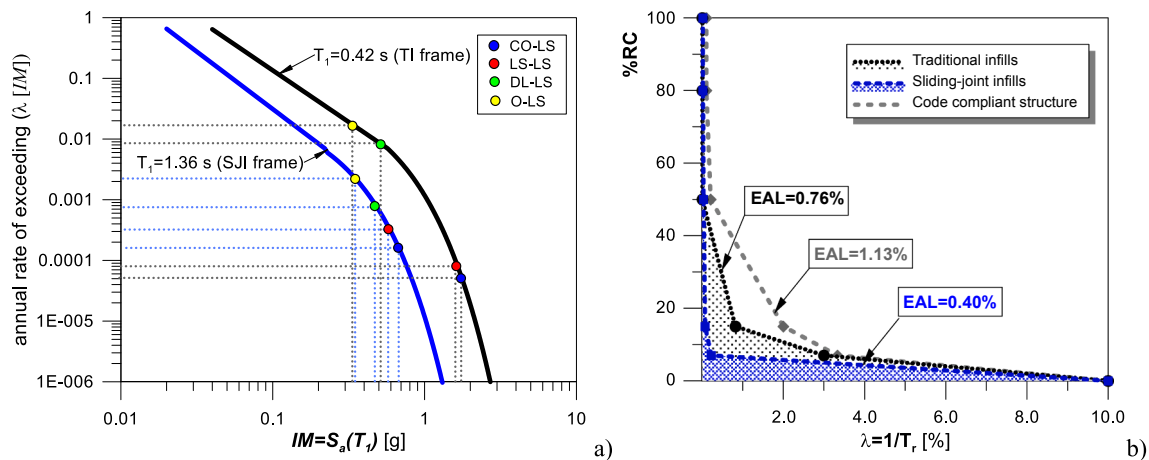


Fig. 24. EAL assessment: (a) determination of λ values associated with $\bar{S}_a = (T_i)$; (b) λ -%RC relationships and EAL for TI frames, SJI frame and code compliant reference structure.

joint infilled frames were very close one to each other and lower than that of TI frame (Fig. 20a). For traditionally infilled frame configuration, this resulted, in O-LS, DL-LS, ISD-LS and FID-LS probabilities of occurrence respectively 10 times, 13 times, 5 times and 6 times the same probabilities obtained in for SJI frames.

- EAL was assessed by using the procedure by Cosenza et al. (2018) [36] with a direct evaluation of the annual rates of exceeding the limit states. For SJI frames EAL was 0.40%, that is about a half with respect to that of traditionally infilled frames (0.76%). This gain is entirely related to the reduced annual rates of exceedance evaluated for non-structural limit states in case of SJI frames.
- Sliding-joint infilled frames resulted an effective design solution to improve reliability and reduce losses during the service life of reinforced concrete of masonry infilled structures. Moreover, the flexibility in their arrangement (number of sliding joints, contact material, sliding joints friction coefficient) leaves space to further improvement in the framework of PBEE.

CRediT authorship contribution statement

Fabio Di Trapani: Conceptualization, Methodology, Writing - review & editing, Supervision. **Valentino Bolis:** Methodology, Formal analysis, Writing - review & editing. **Francesco Basone:** Formal analysis. **Marco Preti:** Conceptualization, Writing - review & editing, Supervision.

Declaration of Competing Interest

We declare that we have no conflict of interest.

Acknowledgements

This study was supported by DPC/ReLUIIS, Rete di Laboratori Universitari di Ingegneria Sismica, WP 10, 2019-2021.

Appendix A. Supplementary material

Supplementary data to this article can be found online at <https://doi.org/10.1016/j.engstruct.2020.110306>.

References

[1] Braga F, Manfredi V, Masi A, Salvatori A, Vona M. Performance of non-structural elements in RC buildings during the L'Aquila, 2009 earthquake. *Bull Earthquake Eng* 2011;9(1):307–24. <https://doi.org/10.1007/s10518-010-9205-7>.
 [2] Polese M, Di Ludovico M, Marcolini M, Protà A, Manfredi G. Assessing reparability: simple tools for estimation of costs and performance loss of earthquake damaged

reinforced concrete buildings. *Earthquake Eng Struct Dyn* 2015;44(10):1539–57.
 [3] De Martino G, Di Ludovico M, Protà A, Moroni C, Manfredi G, Dolce M. Estimation of repair costs for RC and masonry residential buildings based on damage data collected by post-earthquake visual inspection. *Bull Earth Eng* 2017;15(4):1681–706.
 [4] Del Vecchio C, Di Ludovico M, Pampanin S, Protà A. Repair costs of existing RC buildings damaged by the L'Aquila earthquake and comparison with FEMA P-58 predictions. *Earthq Spectra* 2018;34(1):237–63.
 [5] Cavaleri L, Di Trapani F. Prediction of the additional shear action on frame members due to infills. *Bull Earthquake Eng* 2015;13(5):1425–54.
 [6] Di Trapani F, Malavisi M. Seismic fragility assessment of infilled frames subject to mainshock/aftershock sequences using a double incremental dynamic analysis approach. *Bull Earthquake Eng* 2019;17(1):211–35.
 [7] Mosalam KM, Günay S. Progressive collapse analysis of reinforced concrete frames with unreinforced masonry infill walls considering in-plane/out-of-plane interaction. *Earthquake Spectra* 2015;31(2):921–43.
 [8] Varum H, Furtado A, Rodrigues H, Dias-Oliveira J, Vila-Pouca N, Arêde A. Seismic performance of the infill masonry walls and ambient vibration tests after the Ghorka 2015, Nepal earthquake. *Bull Earthquake Eng* 2016; 1–28.
 [9] Triantafillou TC. Strengthening of masonry structures using epoxy-bonded FRP laminates. *J Compos Constr, ASCE* 1998;2(2):96–104.
 [10] Kyriakides MA, Billington SL. Seismic retrofit of masonry-infilled non-ductile reinforced concrete frames using sprayable ductile fiber-reinforced cementitious composites. In: Proc from the 14th world conference on earthquake engineering, Beijing, China, October 12-1; 2008.
 [11] Koutromanos I, Kyriakides M, Stavridis A, Billington S, Shing PB. Shake-table tests of a three-story masonry-infilled RC frame retrofitted with composite materials. *ASCE J Struct Eng* 2013;139(8):1340–51.
 [12] Ezzatfar P, Binici B, Kurc O, Canbay E, Sucuoglu H, Ozece G. Application of mesh reinforced mortar for performance enhancement of hollow clay tile infill walls. *Seismic Eval Rehabil Struct Springer* 2014;26:171–86.
 [13] Marinkovic M, Butenweg C. Experimental and numerical analysis of RC frames with decoupled masonry infills. In: Proceedings of the COMPDYN 2019 7th ECCOMAS thematic conference on computational methods in structural dynamics and earthquake engineering, Crete, Greece; 2019.
 [14] Markulak D, Radić I, Sigmund V. Cyclic testing of single bay steel frames with various types of masonry infill. *Eng Struct* 2013;51:267–77.
 [15] Misir IS. Potential use of locked brick infill walls to decrease soft-story formation in frame buildings. *J Perform Constr Facil* 2015;29:No.5.
 [16] Mohammadi M, Akrami V, Mohammadi-Ghazi R. Methods to improve infilled frame ductility. *J Struct Eng* 2011;137(6):646–53.
 [17] Preti M, Bettini N, Plizzari G. Infill walls with sliding joints to limit infill-frame seismic interaction: large-scale experimental test. *J Earthquake Eng* 2012;16(1):125–41.
 [18] Vailati M, Monti G. Earthquake-resistant and thermo-insulating infill panel with recycled-plastic joints. earthquakes and their impact on society. Springer Natural Hazards, S. D'Amico, ed., Springer International Publishing; 2016. p. 417–32.
 [19] Verlati N, Guidi G, Da Porto F, Modena C. Innovative systems for masonry infill walls based on the use of deformable joints: Combined in-plane/out-of-plane tests. Proceedings of the 16th international brick and block masonry conference, IBMAC 2016. 2016. p. 1359–66.
 [20] Gao X, Stavridis A, Bolis V, Preti M. Experimental study on the seismic performance of non-ductile rc frames infilled with sliding subpanels. In: Proceedings of Eleventh U.S. National Conference on Earthquake Engineering Integrating Science, Engineering & Policy, Los Angeles, California; 2018. p. 12.
 [21] Palios X, Fardis MN, Strepelias E, Bousias SN. Unbonded brickwork for the protection of infills from seismic damage. *Eng Struct* 2017;131:614–24.
 [22] Preti M, Migliorati L, Giuriani E. Experimental testing of engineered masonry infill walls for post-earthquake structural damage control. *Bull Earthquake Eng* 2015;13(7):2029–49.

- [23] Toteov Y, Al Harthy A. Semi interlocking masonry as infill wall system for earthquake resistant buildings: a review. *J Eng Res* 2016;13(1):33–41.
- [24] Bolis V, Stavridis A, Preti M. Numerical investigation of the in-plane performance of masonry-infilled RC frames with sliding subpanels. *J Struct Eng* 2017;143(2):04016168.
- [25] Bolis V, Preti M. Openings in infills with horizontal sliding joints: a parametric study to support the design. *Bull Earthquake Eng* 2019. <https://doi.org/10.1007/s10518-019-00654-9>.
- [26] Manzini CF, Morandi P, Milanese RR, Magenes G. Shaking-table test on a two-storey RC framed structure with innovative infills with sliding joints. In: Proceedings of 16th European conference on earthquake engineering, Thessaloniki, 18-21 June 2018.
- [27] Preti M, Bolis V, Stavridis A. Seismic infill-frame interaction of masonry walls partitioned with horizontal sliding joints: analysis and simplified modeling. *J Earthquake Eng* 2019;23(10):1651–77. <https://doi.org/10.1080/13632469.2017.1387195>.
- [28] Vamvatsikos D, Cornell AC. Incremental dynamic analysis. *Earthq Eng Struct Dyn* 2000;31(3):491–514.
- [29] Cornell CA, Krawinkler H. Progress and challenges in seismic performance assessment. PEER Center News 3. Berkeley: University of California; 2000.
- [30] Maniyar MM, Khare RK, Dhakal RP. Probabilistic seismic performance evaluation of non-seismic RC frame buildings. *Struct Eng Mech* 2009;33:725–45.
- [31] Ribeiro FLA, Barbosa AR, Neves LC. Application of reliability-based robustness assessment of steel moment resisting frame structures under post-mainshock cascading events. *J Struct Eng (ASCE)* 2014.
- [32] Basone F, Cavaleri L, Di Trapani F, Muscolino G. Incremental dynamic based fragility assessment of reinforced concrete structures: stationary vs. non-stationary artificial ground motions. *Soil Dyn Earthquake Eng* 2017;103:105–17.
- [33] Di Trapani F, Bertagnoli G, Ferrotto MF, Gino D. Empirical equations for the direct definition of stress-strain laws for fiber-section-based macromodeling of infilled frames. *J Eng Mech* 2018;144(11):04018101.
- [34] Baker JW. Efficient analytical fragility function fitting using dynamic structural analysis. *Earthquake Spectra* 2015;31(1):579–99.
- [35] Calvi GM. Choices and criteria for seismic strengthening. *J Earthq Eng* 2013;17:769–802.
- [36] Cosenza E, Del Vecchio C, Di Ludovico M, Dolce M, Moroni C, Prota A, et al. The Italian guidelines for seismic risk classification of constructions: technical principles and validation. *Bull Earthquake Eng* 2018;16:5905.
- [37] NTC. Ministry Decree, January 17th, 2018; Norme tecniche per le costruzioni (Technical codes for construction) [in Italian]; 2018.
- [38] Eurocode 8. Design of structures for earthquake resistance—Part 1: general rules, seismic actions and rules for buildings. European Committee for Standardization, Brussels; 2004.
- [39] Preti M, Bolis V. Seismic analysis of a multi-story RC frame with infills partitioned by sliding joints. *Ingegneria sismica*, Vol. Anno XXXIV; 2017; Special Issue.
- [40] McKenna F, Fenves GL, Scott MH, et al.. Open system for earthquake engineering simulation. University of California, Berkeley, CA; 2000.
- [41] Mander JB, Priestley MJ, Park R. Theoretical stress-strain model for confined concrete. *J Struct Eng* 1988;114(8):1804–26.
- [42] Popovics S. A numerical approach to the complete stress strain curve for concrete. *Cem Concr Res* 1973; 3(5): 583–99.
- [43] Campione G, Cavaleri L, Di Trapani F, Giuseppe M, Scaduto G. Biaxial deformation and ductility domains for engineered rectangular RC cross-sections: A parametric study highlighting the positive roles of axial load, geometry and materials. *Eng Struct* 2016;107:116–34. <https://doi.org/10.1016/j.engstruct.2015.10.030>.
- [44] Filippou FC, Bertero VV, Popov EP. Effects of bond deterioration on hysteretic behavior of reinforced concrete joints 1983. 137–47.
- [45] Cavaleri L, Di Trapani F, Macaluso G, Maurizio P. Reliability of code-proposed models for assessment of masonry elastic moduli. *Ing Sismica* 2012;21(1):38–59.
- [46] Asteris PG, Cavaleri L, Di Trapani F, Sarhosis V. A macro-modelling approach for the analysis of infilled frame structures considering the effects of openings and vertical loads. *Struct Infrastruct Eng* 2016; 12(5): 551–66.
- [47] Stavridis A. Analytical and experimental study of seismic performance of reinforced concrete frames infilled with masonry walls. PhD Thesis. eScholarship; 2009.
- [48] Federal Emergency Management Agency (FEMA) Pre-standard and commentary for the seismic rehabilitation of buildings. Report No. FEMA-356, Federal Emergency Management Agency, Washington, DC; 2000.
- [49] Fédération internationale du béton (FIB). Model code 2010: final draft. International Federation for Structural Concrete; 2012.
- [50] Collins MP, Mitchell D. Prestressed concrete structures. Response Publications; 1997.
- [51] Morandi P, Hak S, Magenes G. Performance-based interpretation of in-plane cyclic tests on RC frames with strong masonry infills. *Eng Struct* 2018;156:503–21.
- [52] Cardone D, Perrone G. Developing fragility curves and loss functions for masonry infill walls. *Earthq Struct* 2015;9:257–79 <https://doi.org/10.12989/eas.2015.9.1.257>.
- [53] Iervolino I, Galasso C, Cosenza E. REXEL: computer aided record selection for code-based seismic structural analysis. *Bull Earthquake Eng* 2009;8:339–62.
- [54] Iervolino I, Spillatura A, Bazzurro P. Seismic reliability of code-conforming Italian buildings. *J Earthquake Eng* 2018;22(sup2):5–27.